2008

Microwave nondestructive evaluation of aircraft radomes

David Bennett Johnson
Iowa State University

Microwave nondestructive evaluation of aircraft radomes

by

David Bennett Johnson

A thesis submitted to the graduate faculty

in partial fulfillment of the requirements for the degree of

MASTER OF SCIENCE

Major: Electrical Engineering

Program of Study Committee:
Nicola Bowler, Major Professor
Brian Hornbuckle
David Hsu

Iowa State University

Ames, Iowa

2008

$$\nabla \cdot \vec{D} = \rho$$

$$\nabla \times \vec{E} = -\frac{\partial \vec{B}}{\partial t} = -j\omega\vec{B}$$

$$\nabla \cdot \vec{B} = 0$$

$$\nabla \times \vec{H} = \vec{J} + \frac{\partial \vec{D}}{\partial t} = \vec{J} + j\omega\vec{D}$$

- James Clerk Maxwell & Oliver Heaviside

...men never have been and never will be able to undo or even to control reliably any of the processes they start through action.

- Hannah Arendt, The Human Condition

And so on.

- Kurt Vonnegut, Breakfast of Champions

TABLE OF CONTENTS

LIST OF TABLES

LIST OF FIGURES

Acknowledgements

First and foremost, I would like to thank Dr. Nicola Bowler for her guidance through the entire project. Her eagerness in pursuing an alternate approach to a problem is sincerely appreciated. Additionally, I am most grateful for her continued confidence in my abilities to use expensive equipment in spite of certain electrical insulation related oversights demonstrated during the course of this research. I would also like to give thanks to Dr. John Bowler for his work regarding the open-ended waveguide problem, both with the crafting of a solution and his ability to make an incredibly daunting problem seem somewhat manageable.

I would also like to thank Dr. Robert Weber for his assistance with several technical aspects regarding this project. He cannot be thanked enough for all his help. Additionally, I would like to thank Dr. Dirk Deam for introducing me to an entirely different way of learning, to the importance of the polis, and for being testament to the idea an engineer can pursue interests beyond the realms of physics and mathematics. Dr. Mani Mina's impact and contributions to my undergraduate education cannot go unacknowledged. His passion for teaching and the success of his students, both the classroom and the learning community, goes unmatched. Thank you.

Additionally, I would like to thank my committee for agreeing to dedicate their time to assessing and improving the following work. This material is based upon work supported by the Air Force Research Laboratory under Contract # FA8650-04-C-5228 at Iowa State University's Center for Nondestructive Evaluation.

Finally, I would like to thank my parents, who put up with raising me these past 23 years. I think things turned out alright - kudos.

CHAPTER 1. Introduction

As the aviation industry continues to experience increased demand on maintenance turn-around time with decreased budgets, the airlines in particular seek advances in cost and efficiency for inspection technology. Such improvements not only increase aviation safety, but also lead to significant cost savings and avoidances. One particular inspection need is that of aircraft radomes, often found as the nosecone such as that seen in Figure 1.1, housing the plane's weather radar. This structure, fabricated out of low-loss/permittivity composite materials (such as fiberglass), must appear as "electrically transparent" as possible to the radar. Like a window to the human eye, any variations (in the form of changes in the radome's electrical permittivity) or excess material will make sensing the outside world through the structure difficult. Defects such as water ingression, excess paint, and impact damage hinder the radar's ability to sense accurately. No field-ready technique exists to evaluate the electrical properties or electrical consistency of the radome.

As such, a novel approach using coplanar stripline resonators is considered herein to address this problem. The resonator, consisting of two parallel metal strips deposited on a circuit board, is sensitive to both the permittivity of its substrate as well as whatever material sits on top of the strips. Changes in either one of these parameters will shift the resonant frequency of the resonator. This phenomena can be applied to make a sensor, where the shift in resonant frequency indicates a change in the electrical properties of the test piece. The greater the permittivity of the anomaly, the stronger the shift in resonant frequency. It is the goal of this work to demonstrate the viability of this technique to inspect for defects in aircraft radomes. A more thorough introduction to the problem will be given, followed by an exploration into the theory of microwave propagation from a flanged rectangular waveguide into a dielectric half-

Figure 1.1 Radome installed on an American Airlines aircraft.

space. From there, the design process for the coplanar stripline resonators will be presented. This exploration will conclude with a discussion of the testing and results from the resonator investigation.

1.1 Statement of Problem

Aircraft radomes present a unique set of difficulties and requirements for nondestructive evaluation (NDE). Since its advent during World War II, the radar has been inextricably intertwined with aviation. Both in the air and on the ground, it serves a number of purposes, from tracking enemy aircraft to watching for undesirable weather. Often times, the antenna used by the radar requires some form of protection and shielding, guarding it from the elements, and in the case of aircraft, eliminating wind loading on the antenna and reducing wind resistance on the aircraft. This cover is known as a radome. On an aircraft, the nose cone typically serves as the radome for the plane's weather radar, shown in Figure 1.2.

1.1.1 Quality control

In order for the radar to function correctly, the radome must appear as 'electrically transparent' as possible while maintaining a high degree of uniformity. As such, the structure must

Figure 1.2 C-band radome from a Boeing 727.

fit within tight specifications dictated by the design and frequency of the radar. This not only includes the structure (constructed from a composite material), but also the paint applied to the outer surface. The outer and inner surfaces are generally made from a fiberglass sheet; these surfaces are separated by some type of core. Presently, the core is comprised of either a solid foam core or a composite honeycomb structure. Fluted core radomes (continous channel) were once used, however they are now considered obsolete due to high manufacturing costs [CNDE, 2007]. Any variations in paint or structural thickness, as well as discontinuities within the core, will alter the transmitted/received radiation patterns (sometimes referred to as the radome signature). Factors such as excess resin from the composite assembly which typically pose no issue in most applicaions become relevant. With such a demand for perfection, quality control at the manufacturing level becomes critical.

1.1.2 Deployment incurred damange

Once deployed in the field, the radome's signature may change. Most often, this change results from damage to the structure. Impact damage (hail, birds, etc.) ranges anywhere from

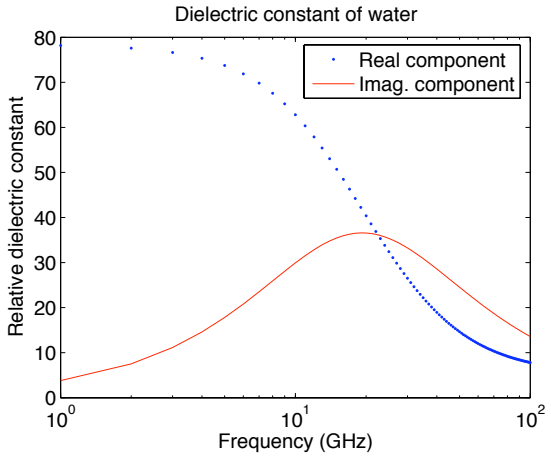

Figure 1.3 Plot of the complex permittivity of water at 25° C.

a disbond between the outer layers and the composite core to a complete crack or fracture of the material. Damage from a lightning strike or static discharge may burn small holes in the structure. Both cases will affect the transmission and reception of RF signals. However, the direct effect of these two damages is minor compared to their indirect effect. Whenever the outer layer of a radome becomes penetrated, it allows for the ingression of water within the structure, causing a significant variation to the material's electric properties. A radome's relative dielectric constant ranges between 2 and 4 [Rao, 1989]. With a typical weather radar operating in the X-band (8-12 GHz) [Collins, 2008], the relative dielectric constant for water is $62.8 + j29.93$ (at 10 GHz) for a temperature of 25°C [Press, 2004], as shown in Figure 1.3.

With the significant contrast between the permittivity of water and air, the presence of water drastically alters the radome's signature. A simulation of the water ingression's impact on the signature with a 10 GHz signal may be seen in Figure 1.4. This was performed using a finite difference, time domain (FDTD) simulation written in MATLAB. A summary of the various parameters of the simulation may be found in Table 1.1. The left column of images in Figure 1.4 show a radome with 1 cc of water present; the middle is the same radome without the water; the right shows the difference between the two - effectively it shows the effect of the water's presence. The location of the ingression may be noticed in all three of the images on the right. Additionally, a faint outline of the honeycomb structure (in the right side of the

Parameter	Value
Frequency (f)	10 GHz
Spacial step size (dx)	1 mm
Time step size (dt)	1.667 ps
x-dimension grid size (N_x)	200 units
y-dimension grid size (N_y)	101 units

Table 1.1 Details for FDTD simulation of water ingression inside a radome structure.

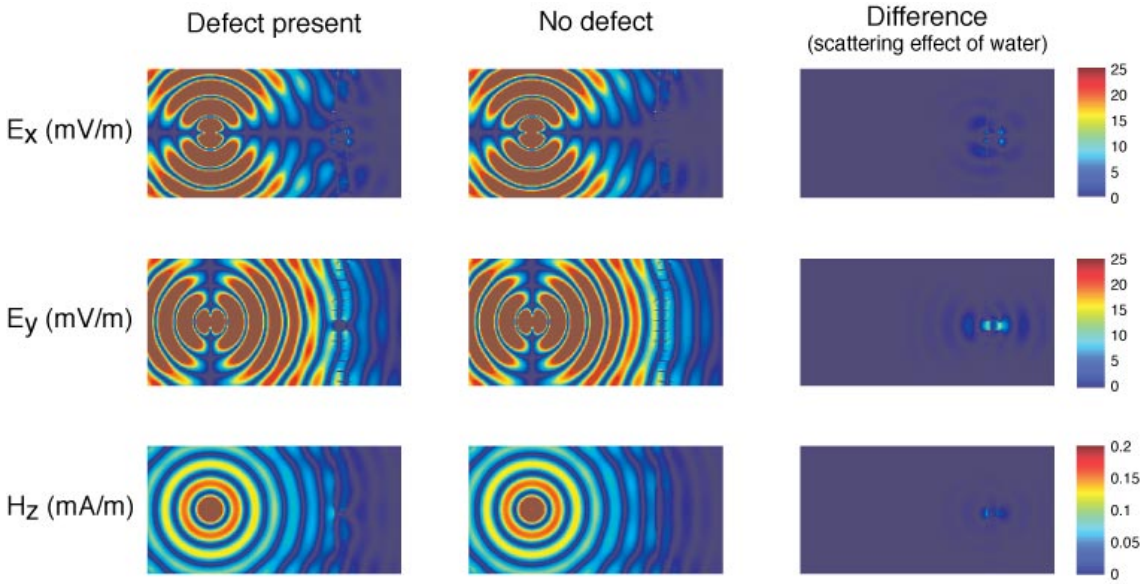

Figure 1.4 Electric and magnetic fields (10 GHz) propagating through a honeycomb-cored radome with a 1 cc water ingression (left), without the water ingression (center), and the different between the two (right).

simulated area) is shown in the E_y plots in Figure 1.4 . The E_y plot (center right) clearly shows the ingression acting as a radiator, scattering the incident microwave energy. From the perspective of the weather radar, the altered signal that it receives will provide weather information that is either skewed or completely invalid.

In addition to the electrical effect, the water's presence could potentially cause further damage to the radome's structure from the expansion and contraction of the freezing and thawing water. Up to 85% of radome repairs and retirements may be attributed to water ingression [Blatz et al., 2007]. As such, detection of both impact damage and water ingression becomes a vital need once put into service.

Class	Average efficiency
A	90% (no area lower than 85%)
B	87% (no area lower than 82%)
C	84% (no area lower than 78%)
D	80% (no area lower than 75%)
E	70% (no area lower than 55%)

Table 1.2 Radome performance classes as prescribed under RCTA/DO-213.

1.1.3 Radome repair

When a problem is found on a radome (such as a burn hole or impact damage), a repair may be attempted. Often, this is completed by either filling the flaw with putty/potting compound or replacing the damaged sections of the core and outer layer [Atlanta Aerospace, 2008]. The integrity of this repair is critical on both the physical and electrical levels. Physically, the repair must maintain the original level of structural integrity and form a secure seal with the bulk of the body to prevent moisture ingression. Electrically, the permittivity of the repaired area must match that of the rest of the structure. The new permittivity for the structure not only depends upon the repair, but also the thickness of the newly applied paint.

The process used for repair varies by vendor. One repair procedure, used by Atlanta Aerospace, demonstrates a significant number of steps. Among these, the radome undergoes a visual inspection, tap test (discussed in 1.2.5), transmissivity test, complete coating/paint removal followed by a moisture test, and replacement of the damaged areas [Atlanta Aerospace, 2008]. The transmissivity test generally requires the mounting of the radome in an anechoic chamber (simulating free space), transmitting a signal through the radome, and measuring the amount of signal loss due to the radome. Comparing the strength of the signal after attenuation by the radome to an uninhibited signal yields the "efficiency" of the radome. After a repair, the radome undergoes a second transmissivity test and is reclassified based on its performance. The classification criteria is shown in Table 1.2.

Thus, there exists a wide array of NDE needs through the life of the radome. Prior to shipment from the factory, it must pass a number of quality control checks. Once deployed, it much be regularly inspected for both impact damage as well as water ingression. As such, an

ideal inspection system must detect water ingression, paint thickness consistency, and repair continuity.

1.2 Present Methods of Radome NDE

Several methods for inspecting radomes are already used in industry. No single technique provides an all-encompassing solution to the NDE needs of this particular application. Operators use thermography and radome moistures meters for detecting water in radomes while ultrasonic techniques are used for detecting disbonds. The following provides an overview of the existing techniques.

1.2.1 Radome moisture detection equipment

One popular method consists of using a handheld moisture detector to scan the exterior of the radome such as the Aqua A8-AF radome moisture meter. The A8-AF in particular measures the "radio frequency dielectric power loss." Available product documentation does not provide any further details on the specific frequencies of operation. Despite the fact this equipment is specifically designed for use on radomes, the equipment is not extremely sensitive [Blatz et al., 2007] and may show a false positive from antistatic paint that is too conductive [Napert, 1999]. Additionally, this will not provide a strong indication regarding paint thickness on the radome.

1.2.2 Thermography

Another technique is thermography, where the radome is heated and left to cool in view of an infrared camera. The camera notes changes in the rate of cooling along the radome surface. Unfortunately, this often cannot detect features such as paint thickness.

1.2.3 Electromagnetic Infrared (EMIR) method

Similar to thermography, this technique uses an infrared camera to detect changes in the radome's properties. However, with this technique a thin film of photothermal converter is

placed on one side of the radome while an X-band microwave source illuminates the other [Balageas et al., 2000]. The incident microwave radiation will heat any water ingression present in the radome. The EMIR technique has the implied disadvantage that the radome must be removed of the aircraft and taken to a controlled setting. Additionally, it may be difficult for a subtle variation such as paint thickness to appear in the measurements.

1.2.4 Ultrasonics

This technique works primarily for detecting disbonds in the structure. Using an air-coupled transmission technique, it has the advantage of having a higher degree of resolution, however it has been noted that a fair amount of difficulty exists when attempting to identify critical damage because the transmitted amplitude is very low compared to normal delaminations [Balageas et al., 2000].

Additionally, this technique cannot evaluate the dielectric properties of the radome. The properties that affect ultrasonic measurements, things such as acoustic impedance, do not necessarily correspond to dielectric properties. For example, an excess of paint (e.g. 0.1 mm) on a particular portion of the radome might show up for a microwave-based measurement, but not have a (noticeable) impact on an ultrasonic scan.

1.2.5 Tap test

Tap testing is a common method for inspecting for delamination in composite materials. With this test, the inspector listens for changes in the sound of a tap on the surface in question. A void will make a different sound compared to a delamination. This techique is highly subjective, making it useful as a first step in an inspection [Wegman and Tullos, 1992]. Like the other techniques listed above, this will not provide any indication about the paint thickness on the radome.

Capable of application in form of handheld unit
Useable on installed radome
Detects water ingressions (greater than 0.1 cc)
Indicates paint thickness variations of 1 mil or more

Table 1.3 List of criteria for microwave NDE technique applied to aircraft radomes.

1.3 Proposed Method

As no presently used NDE method fully addresses all the electrical defects found in aircraft radomes (water ingression, paint thickness, etc) in a field-testable manner, an alternate technique is suggested. Since the very issue under consideration centers around the structure's performance with microwave frequency radiation, it would make sense to use such as a basis for inspection. The chosen technique should meet the baseline criteria presented in Table 1.3.

1.3.1 Open-ended rectangular waveguide

Over the past few decades, single-sided (reflection) microwave NDE techniques using rectangular waveguides have matured greatly, finding a variety of applications in multiple industries. These range from concrete testing [Khanfar et al., 2003, Nadakuduti et al., 2003, Nadakuduti et al., 2006] to inspecting carbon-loaded composite structures [Saleh et al., 2003, Kharkovsky et al., 2006] to searching for cracks in metals [Ganchev et al., 1996, Saka et al., 2002]. In these processes, a vector network analyzer measures the complex reflection coefficient of a waveguide mounted above the sample's surface, similar to that shown in Figure 1.5. Changes in the dielectric properties of the test-piece will create a different reflection, indicating the presence of a defect. In some applications, the phase and magnitude data are compared to a 'baseline' to determine whether a defect exists. In others, the reflection coefficent is used to extract the material's dielectric constant, allowing one to quantitatively characterize a given sample.

This technique was researched by Bell Helicopter, in conjunction with Systems and Materials Research Consultancy, for use in measuring coating thickness on rotor blades. This work

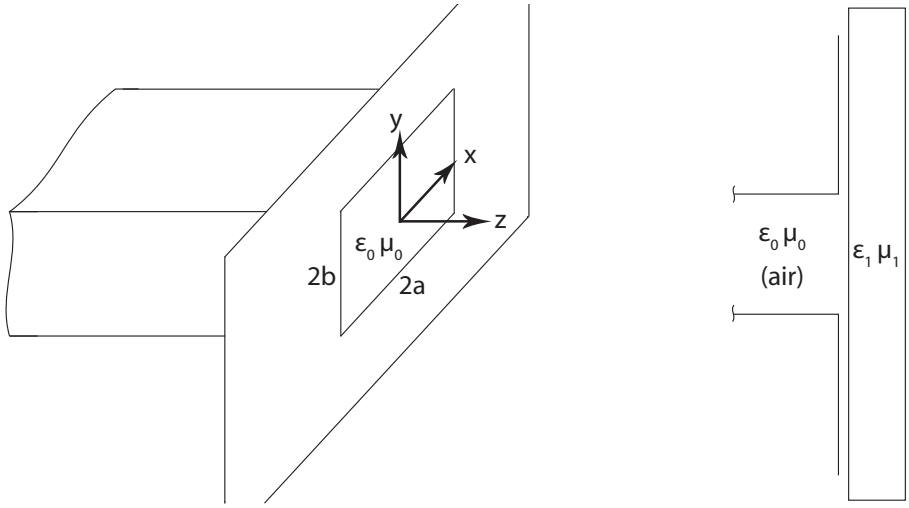

Figure 1.5 Open-ended waveguide with flange (left) and a waveguide with flange applied to a test-piece (right).

yielded a handheld device that delivers a "go/no go" indication to the inspector. However, this system requires the substrate material to be a metal or some other conductive material (such as carbon fiber) [Nissen, 2005].

Unfortunately, the waveguide technique proves problematic in several respects for radome inspections. First, due to the low-loss/permittivity nature of the application, a technique based on the reflection of microwave energy will be highly susceptible to noise. The interior of the radome, during an inspection might need to be backed by a conductor of some kind to reflect the energy back to its source. If some quantifiable measurement is desired (i.e. finding the effective permittivity of the material), the waveguide itself would also need a relatively large flange to obtain precise measurements. This is to eliminate any non-ideal interactions between the test-piece and the body of the waveguide.

Additionally, although the measurements obtained from the technique provide great insight into the electrical properties of the test-piece, the measurements themselves are unwieldy for collection in the field. Work by Stewart et al. [Stewart et al., 2007] recently demonstrated successful measurements employing a portable network analyzer, however as stated above the flange on the waveguide needs to be relatively large to ensure sound measurements. Finally, due to the requirement of a vector network analyzer, this technique becomes quite costly,

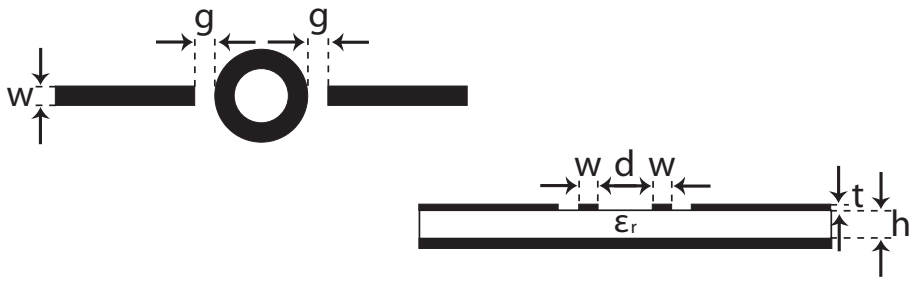

Figure 1.6 Schematic diagram of a ring resonator.

making its viability as a solution even more unlikely.

1.3.2 Microstrip resonators

Aside from the waveguide reflection method, various geometries of microstrip resonators have been use for materials evaluation. Ring resonators, similar to that shown in Figure 1.6, have been well characterized for the inspection of moisture content in agricultural products [Joshi et al., 1997, Abegaonkar et al., 1999b]. In this application, the grain/leaf was placed on top of the sensor (microstrips affixed to a circuit board substrate) and the resonant frequency is measured. This frequency is compared to the resonant frequency without a test-piece. This shift would indicate the amount of moisture in the test-piece. Similarly, stripline and coplanar waveguide resonators have been applied to determine the dielectric properties of various materials [Kent, 1972, Kent and Kohler, 1984, Waldo et al., 1997, Hu et al., 2006, Tan et al., 2004, Tsuji et al., 2007]. It should be noted that when used for dielectric film measurements, the application is inherently destructive as it requires direct deposition of the resonator on the surface of the material under test. In all of these applications, the changing dielectric properties (due to change in moisture content) of the material under test cause a shift in the resonant frequency of the stripline/coplanar waveguide resonator.

The advantage to this particular technique is that it does not require phase measurements, allowing for the use of a spectrum analyzer (or custom designed circuitry), greatly reducing the overall cost of the measurement system when compared to the techniques employing a vector network analyzer. Additionally, since the size of the resonator is on the order of a centimeter, the sensor could easily be fabricated into a handheld device for spot inspections or assembled

in an array configuration for rapid inspections.

Over the next two chapters, various aspects of the waveguide and the microstripmethods will be considered. In Chapter 2, a detailed review will be presented of a solution put forth by Bois et al. [Bois et al., 1999] for an infinite-flanged retangular waveguide directed toward a dielectric half-space. In Chapter 3, the design and testing of a coplanar stripline resonator sensor will be discussed.

CHAPTER 2. Open-Ended Rectangular Waveguide

2.1 Introduction to the Open-Ended Rectangular Waveguide Half-Space Problem

The problem of a waveguide directed into an infinite dielectric halfspace (shown in Figure 2.1) is not a recent problem. Several works have tackled similar configurations. Using numerical techniques, Mautz and Harrington [Mautz and Harrington, 1978] modeled a waveguide with an infinite flange directed into an infinite half-space. This basic situation was analytically modeled by Yoshitomi and Sharobim [Yoshitomi and Sharobim, 1994]. A number of other works sought analytical solutions to similar situations, including a waveguide directly applied to a lossy finite material with a conductor backing [Stewart and Havrilla, 2006]. Going a step further in complexity, Baker-Jarvis et al. [Baker-Jarvis et al., 1994] analyzed a coaxial probe with an air gap between the probe aperture and a dielectric of finite thickness, terminated by either an infinite dielectric half-space or perfect electric conductor (PEC). An article by Bois et al. [Bois et al., 1999], relying heavily on same methods found in [Yoshitomi and Sharobim, 1994], presents the exact situation to be considered herein. However, the derivation presented in [Bois et al., 1999] lacks consistency in formulation and rigor in detail. As such, this section shall review the various issues found in [Bois et al., 1999], providing a solution with greater detail and a more explicit description of the methodology used.

2.2 Methodology of derivation

The chosen strategy centers on the use of Fourier transforms, following much the same formulation as [Yoshitomi and Sharobim, 1994]. However, before exploring said formulation,

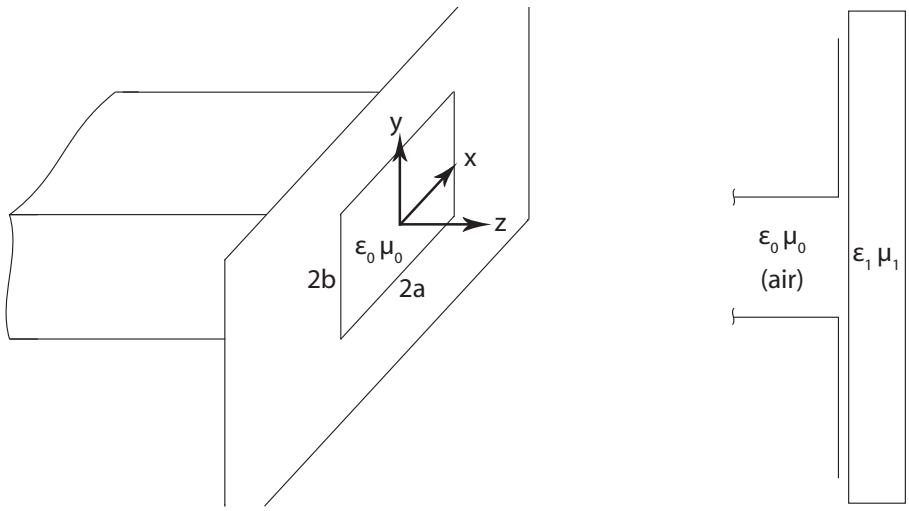

Figure 2.1 Open-ended waveguide with flange (left) and a waveguide with flange applied to a test-piece (right).

one needs to know the basic set of boundary conditions and governing equations. Since the waveguide lies flush with the dielectric (i.e. no air gap), the boundary conditions for this particular problem include the waveguide's walls and the probe-dielectric interface. It is assumed that the walls of the waveguide, as well as the flange on the end of the waveguide, are PECs, and that the flange extends infinitely in the x and y directions. Inside the waveguide,

$$\bar{E}^{wg}_{x,y} = \bar{E}^{i}_{x,y} + \bar{E}^{r}_{x,y} \tag{2.1}$$

$$\bar{H}^{wg}_{x,y} = \bar{H}^{i}_{x,y} + \bar{H}^{r}_{x,y} \tag{2.2}$$

where the superscripts i and r denote the incident and reflected components. Additionally, the superscript t will be used to denote the transmitted field component. At the probe-dielectric interface ($z = 0$), the tangential components of the fields in each region must match, resulting in

$$\bar{E}^{t}_{x,y}(x,y,0) = \begin{cases} \bar{E}^{i}_{x,y}(x,y,0) + \bar{E}^{r}_{x,y}(x,y,0) & \text{for } |x| \le a \text{ and } |y| \le b, \\ 0 & \text{elsewhere} \end{cases} \tag{2.3}$$

$$H^{t}_{x,y}(x,y,0) = \frac{1}{4\pi^2}\int_{-\infty}^{\infty}\int_{-\infty}^{\infty} \tilde{H}^{t}_{x,y}(\xi,\eta)e^{-j(\xi x+\eta y)}\,d\xi\,d\eta = H^{wg}_{x,y}(x,y,0) \tag{2.4}$$

The tangential field component of the electric field is zero on the flange as it is assumed to be an infinite PEC; conversely, the tangential component of the magnetic field is not zero due to surface currents on the flange (i.e. the electric field's normal component is not zero). $\tilde{H}^t_{x,y}(\xi,\eta)$ represents the two-dimensional Fourier transform of $H^t_{x,y}(x,y,0)$. The Fourier transform is given by

$$\tilde{f}(\xi,\eta) = \int_{-\infty}^{\infty}\int_{-\infty}^{\infty} f(x,y)e^{j(\xi x+\eta y)}\,dx\,dy \tag{2.5}$$

and the inverse Fourier transform is given by

$$f(x,y) = \frac{1}{4\pi^2}\int_{-\infty}^{\infty}\int_{-\infty}^{\infty} \tilde{f}(\xi,\eta)e^{-j(\xi x+\eta y)}\,d\xi\,d\eta. \tag{2.6}$$

Assuming the waveguide operates in the fundamental TE_{10} mode, the fields incident to the aperture are described by the magnetic Hertzian vector [Yoshitomi and Sharobim, 1994]

$$\bar{\Pi}^{ih}(x,y,z) = \frac{A^i}{(k_o^2 Z_o)}\cos a_1(x+a)e^{-jk_{10}z}\hat{a}_z \tag{2.7}$$

with wave number $k_o = \sqrt{\mu_o\epsilon_o}$ and intrinsic impedance $Z_o = \sqrt{\mu_o/\epsilon_o}$, where μ_o and ϵ_o are the permeability and permittivity of free space (respectively). The vector potential (2.7), when applied with the following relationship between the vector potentials and the electric and magnetic fields

$$\bar{E} = \bar{\nabla}(\bar{\nabla}\cdot\bar{\Pi}^e) + k_1^2\bar{\Pi}^e - j\omega\mu\bar{\nabla}\times\bar{\Pi}^h \tag{2.8}$$

$$\bar{H} = \bar{\nabla}(\bar{\nabla}\cdot\bar{\Pi}^h) + k_1^2\bar{\Pi}^h + j\omega\epsilon\bar{\nabla}\times\bar{\Pi}^e, \tag{2.9}$$

where $k_1 = \sqrt{\mu\epsilon}$ is the wave number and μ and ϵ are the permeability and permittivity of the medium (respectively), will yield $\bar{E}^i$ and $\bar{H}^i$ [Yoshitomi and Sharobim, 1994]. Likewise, the fields reflected at the waveguide aperture, $\bar{E}^r$ and $\bar{H}^r$, may be calculated using (2.8) and (2.9) on the vector potentials [Yoshitomi and Sharobim, 1994]

$$\bar{\Pi}^{re}(x,y,z) = \sum_{m,n=1}^{\infty}\frac{A^e_{m,n}}{k_o^2}\sin a_m(x+a)\sin b_n(y+b)e^{jk_{mn}z}\hat{a}_z \tag{2.10}$$

$$\bar{\Pi}^{rh}(x,y,z) = \sum_{\substack{m,n=0\\ m=n\neq 0}}^{\infty}\frac{A^h_{m,n}}{k_o^2 Z_o}\cos a_m(x+a)\cos b_n(y+b)e^{jk_{mn}z}\hat{a}_z \tag{2.11}$$

with $a_m = m\pi/(2a)$, $b_n = n\pi/(2b)$, and $k_{mn} = \sqrt{k_o^2 - a_m^2 - b_n^2}$. The variables A^e_{mn} and A^h_{mn} are unknown coefficients. The summation accouts for the number of possible discrete modes which may be reflected off the half-space into the waveguide. It should be noted, [Bois et al., 1999] mistakenly replaced $\cos b_n(y+b)$ with $\sin b_n(y+b)$ in (2.11). Similarly, the transmitted fields are represented by the vector potentials [Bois et al., 1999]

$$\bar{\Pi}^{te}(x,y,z) = \frac{1}{4\pi^2}\int_{-\infty}^{\infty}\int_{-\infty}^{\infty}\frac{A^e(\xi,\eta)}{k_1^2}e^{-j(\xi x+\eta y+\zeta z)}\hat{a}_z\,d\xi\,d\eta \tag{2.12}$$

$$\bar{\Pi}^{th}(x,y,z) = \frac{1}{4\pi^2}\int_{-\infty}^{\infty}\int_{-\infty}^{\infty}\frac{A^h(\xi,\eta)}{k_1^2 Z_1}e^{-j(\xi x+\eta y+\zeta z)}\hat{a}_z\,d\xi\,d\eta \tag{2.13}$$

where $\zeta = \sqrt{k_1^2 - \xi^2 - \eta^2}$, k_1 and Z_1 are the respective wave number of the wave in the dielectric and impedance of the dielectric, and $A^{e,h}(\xi,\eta)$ are the unknown spectral functions. The transmitted potentials are no longer constrained by the boundary conditions present in the waveguide, so there are an infinite number of possible modes yielding an infinite integral rather than a summation. Additionally, the elimination of the waveguide walls removes the sine and cosine terms.

With the basic field formulations known, efforts may now shift toward the approach for finding the unknown coefficients A^e_{mn} and A^h_{mn} that describe the unknown fields in the waveguide. Because of the form of (2.12) and (2.13), the application of the Fourier transform allows solving for the spectral functions $A^{e,h}(\xi,\eta)$. Once obtained, one may then substitute the resulting equation for $\tilde{H}^t$ into (2.4). Due to the boundary conditions on the waveguide walls, both sides are then multiplied by $\sin a_p(x+a)\cos b_q(y+b)$ for the x component, or $\cos a_p(x+a)\sin b_q(y+b)$ for the y component, and integrating over the dimensions of the waveguide results in two sets of linear equations from which A^e_{mn} and A^h_{mn} can be obtained. The rationale behind these steps was never mentioned in either [Yoshitomi and Sharobim, 1994] or [Bois et al., 1999].

In order to find $A^{e,h}(\xi,\eta)$ for the transmitted field, the tangential electric field continuity equation,

$$E^t_{x,y}(x,y,0) = \frac{1}{4\pi^2}\int_{-\infty}^{\infty}\int_{-\infty}^{\infty}\tilde{E}^t_{x,y}(\xi,\eta)e^{-j(\xi x+\eta y)}\,d\xi\,d\eta = E^{wg}_{x,y}(x,y,0) \tag{2.14}$$

shall be used in conjunction with (2.8). For the purpose of simplification, the Fourier transform (given by 2.5) shall be taken on both sides of (2.14), yielding $\tilde{E}^t_{x,y}(\xi,\eta) = \tilde{E}^{wg}_{x,y}(\xi,\eta)$.

Because the continuity equation at $z = 0$ only contains components tangential to the waveguide flange, (2.8) simplifies to

$$\bar{E}_{x,y} = \bar{\nabla}_{tan}(\bar{\nabla}_{tan} \cdot \bar{\Pi}^e) + k_1^2\bar{\Pi}^e - j\omega\mu\bar{\nabla}_{tan} \times \bar{\Pi}^h \tag{2.15}$$

where $\nabla_{tan} = \partial/\partial x\hat{a}_x + \partial/\partial y\hat{a}_y$. Using ∇_{tan} to take the curl of both sides of Equation 2.15, one can then solve for

$$A^h(\xi,\eta) = \frac{k_1\left[\xi\tilde{E}^{wg}_y(\xi,\eta) - \eta\tilde{E}^{wg}_x(\xi,\eta)\right]}{(\xi^2+\eta^2)}. \tag{2.16}$$

Likewise, taking the tangential divergence of (2.14) yields

$$A^e(\xi,\eta) = \frac{-k_1^2\left[\xi\tilde{E}^{wg}_x(\xi,\eta) + \eta\tilde{E}^{wg}_y(\xi,\eta)\right]}{\zeta(\xi^2+\eta^2)}. \tag{2.17}$$

Knowing $A^e(\xi,\eta)$ and $A^h(\xi,\eta)$, the equations for $\tilde{H}^t_x$ and $\tilde{H}^t_y$ can be found using (2.9), (2.12), and (2.13), giving

$$\begin{aligned}\tilde{H}^t_x(\xi,\eta) &= \frac{-\left[\xi\eta\tilde{E}^{wg}_x(\xi,\eta)+(k_1^2-\xi^2)\tilde{E}^{wg}_y(\xi,\eta)\right]}{\zeta k_1^2 Z_1} \\ &= \frac{-\xi\eta\left[\tilde{E}^i_x(\xi,\eta)+\tilde{E}^r_x(\xi,\eta)\right]+(k_1^2-\xi^2)\left[\tilde{E}^i_y(\xi,\eta)+\tilde{E}^r_y(\xi,\eta)\right]}{\zeta k_1^2 Z_1}\end{aligned} \tag{2.18}$$

and

$$\begin{aligned}\tilde{H}^t_y(\xi,\eta) &= \frac{(k_1^2-\eta^2)\tilde{E}^{wg}_x(\xi,\eta)+\xi\eta\tilde{E}^{wg}_y(\xi,\eta)}{\zeta k_1^2 Z_1} \\ &= \frac{(k_1^2-\eta^2)\left[\tilde{E}^i_x(\xi,\eta)+\tilde{E}^r_x(\xi,\eta)\right]+\xi\eta\left[(E^i_y(\xi,\eta)+\tilde{E}^r_y(\xi,\eta)\right]}{\zeta k_1^2 Z_1}.\end{aligned} \tag{2.19}$$

The left-hand side of the magnetic continuity equation (2.4) can now be put in terms of $E^{wg}_{x,y}$. To solve the right-hand side, (2.4) is multiplied by $\sin a_p(x+a)\cos b_q(y+b)$ (for H^r_x) or $\cos a_p(x+a)\sin b_q(y+b)$ (for H^r_y) and is integrated over the cross-section of the waveguide aperture. Using (2.9) as well as (2.10) and (2.11), one can find an expression for $H^r_{x,y}$. This

results in

$$\int_{-a}^{a}\int_{-b}^{b} H_x^r(x,y,0)\sin a_p(x+a)\cos b_q(y+b)dydx$$
$$= j\frac{ab}{Z_o k_o^2}(k_o b_q A_{pq}^e - k_{pq}A_{pq}^h a_p(1+\delta_{0q})) \tag{2.20}$$

for $p = 1, 2, 3, ...$ and $q = 0, 1, 2, ...$, and

$$\int_{-a}^{a}\int_{-b}^{b} H_y^r(x,y,0)\cos a_p(x+a)\sin b_q(y+b)dydx$$
$$= -j\frac{ab}{Z_o k_o^2}(k_o a_p A_{pq}^e + k_{pq}A_{pq}^h b_q(1+\delta_{0p})) \tag{2.21}$$

for $p = 0, 1, 2, ...$ and $q = 1, 2, 3, ...$ where δ is a Kronecker delta function. The Kronecker delta function appears due to the mismatch between the summations for Π^{re} and Π^{rh} for the permitted modes. It may also be noted that p (q) may go down to zero, even though A_{pq}^e (A_{pq}^h) does not exist at $p = 0$ ($q = 0$), due to the fact a_m (b_q) equals zero, thus nulling the term. The last remaining piece of the equation, the $H_{x,y}^i$ term, can be solved using (2.7) in conjunction with either (2.8) or (2.9), resulting in

$$H_x^i(x,y,0) = -\frac{k_{10}}{k_0 Z_0}E_y^i(x,y,0) = j\frac{a_1 k_{10}}{Z_o k_o^2}A_i \sin a_1(x+a) \tag{2.22}$$

and

$$H_y^i(x,y,0) = E_x^i(x,y,0) = 0. \tag{2.23}$$

Using the same method from above, equation (2.4) is multiplied by $\sin a_p(x+a)\cos b_q(y+b)$, substituting (2.20), (2.21), and (2.22) for H^r and H^i, and is integrated over the aperture. This, when combined with (2.18), yields the final set of equations:

$$\sum_{m,n=1}^{\infty} k_{mn}A_{mn}^e[a_m I_1(x,y,p,q) + b_n I_2(x,y,p,q)]\cdots$$
$$+ \sum_{\substack{m,n=0\\ m=n\neq 0}}^{\infty} k_o A_{mn}^h[b_n I_1(x,y,p,q) - a_m I_2(x,y,p,q)]$$
$$= a_1 A^i\left[k_o I_2(1,0,p,q) - 2k_{10}\frac{Z_1}{Z_0}ab\delta_{1p}\delta_{0q}\right]$$
$$-ab\frac{Z_1}{Z_0}\left[k_o b_q A_{pq}^e - k_{pq}A_p q^h a_p(1+\delta_{0q})\right] \tag{2.24}$$

for $p = 1, 2, 3, ...$ and $q = 0, 1, 2, ...$ and

$$\begin{aligned}
&\sum_{m,n=1}^{\infty} k_{mn} A^e_{mn} [a_m I_3(x, y, p, q) + b_n I_4(x, y, p, q)] \\
&+ \sum_{\substack{m,n=0 \\ m=n\neq 0}}^{\infty} k_o A^h_{mn} [b_n I_3(x, y, p, q) - a_m I_4(x, y, p, q)] \\
&= a_1 A^i k_0 I_4(1, 0, p, q) - ab \frac{Z_1}{Z_0} \left[k_0 a_p A^e_{pq} + k_{pq} b_q A^h_{pq} (1 + \delta_{0p}) \right]
\end{aligned} \tag{2.25}$$

for $p = 0, 1, 2, ...$ and $q = 1, 2, 3, ...$ with

$$I_1(m, n, p, q) = \frac{1}{4\pi^2} \int_{-\infty}^{\infty} \int_{-\infty}^{\infty} \frac{\xi\eta}{\zeta k_1} C^a_m(-\xi) S^b_n(-\eta) S^a_p(\xi) C^b_q(\eta) d\xi d\eta \tag{2.26}$$

$$I_2(m, n, p, q) = \frac{1}{4\pi^2} \int_{-\infty}^{\infty} \int_{-\infty}^{\infty} \frac{k_1^2 - \xi^2}{\zeta k_1} S^a_m(-\xi) C^b_n(-\eta) S^a_p(\xi) C^b_q(\eta) d\xi d\eta \tag{2.27}$$

$$I_3(m, n, p, q) = \frac{1}{4\pi^2} \int_{-\infty}^{\infty} \int_{-\infty}^{\infty} \frac{k_1^2 - \eta^2}{\zeta k_1} S^a_m(-\xi) C^b_n(-\eta) C^a_p(\xi) S^b_q(\eta) d\xi d\eta \tag{2.28}$$

$$I_4(m, n, p, q) = \frac{1}{4\pi^2} \int_{-\infty}^{\infty} \int_{-\infty}^{\infty} \frac{\xi\eta}{\zeta k_1} S^a_m(-\xi) C^b_n(-\eta) C^a_p(\xi) S^b_q(\eta) d\xi d\eta \tag{2.29}$$

and

$$S^a_m(\xi) = \int_{-a}^{a} \sin a_m(x + a) e^{-j\xi z} dx \tag{2.30}$$

$$C^a_m(\xi) = \int_{-a}^{a} \cos a_m(x + a) e^{-j\xi z} dx \tag{2.31}$$

$$S^b_n(\eta) = \int_{-b}^{b} \sin b_n(y + b) e^{-j\eta y} dx \tag{2.32}$$

$$C^b_n(\eta) = \int_{-b}^{b} \cos b_n(y + b) e^{-j\eta y} dx. \tag{2.33}$$

From this point, the coefficients A^e_{mn} and A^h_{mn} may be found using numerical techniques such as the Gaussian quadrature method.

The results (2.24) and (2.25) match those found in [Bois et al., 1999]. It remains to be demonstrated that (2.26), (2.27), (2.28), and (2.29) may be simplified into a form resembling Green's kernel, something neglected in prior studies. A solution found using Green's second theorem will resemble the result found by Stewart and Havrilla [Stewart and Havrilla, 2006] who used Love's equivalence principle.

Further work is needed to consider a variety of situations, each growing in complexity. Investigation could proceed to consider a dielectric slab of finite thickness backed by a conductor, moving on to include lift-off between the probe and the dielectric. The logical culmination with analysis of a conductor-backed, layered, dielectric structure.

With the increase in complication of the problem, so too does its applicability to practical issues. In particular, the final situation mentioned, that of the layered dielectric structure, arises in may different NDE applications, such as evaluating composite materials. The inclusion of a conductor backing allows for greater accuracy in capturing experimental data for structures with a low dielectric constant, such as a radome, so its addition to the model would help to correspond emperical data to the theoretical work, allowing for greater understanding of the single-sided microwave NDE technique for this particular application.

2.3 Open-Ended Rectangular Waveguide Testing

For the purpose of validating the theory presented previously, a benchmark experiment is proposed. Using a rectangular waveguide with a flange attached connected to a vector network analyzer, a sample of lossy material (such as Arc Tecnologies LS-10055) should be characterized. The choice of a lossy material arises from the approximation of the infinite dielectric sheet. If a low-loss/conductivity material is tested, the flange size must be even larger due to the fact much of the radiated energy will propagate a considerable distance before being noteably attenuated. As such, the wave propagating in the plane of the dielectric will eventually hit the edge of the sheet, an air-dielectric boundary. This will introduce a set of reflections otherwise not found in an infinite sheet. After a literature search, no articles were found directly addressing this issue. The works that were found

[Bakhtiari et al., 1993, Stewart and Havrilla, 2006] used a lossy dielectric as their sample, so the air-dielectric boundary condition did not pose as significant of a factor since the wave would be well attenuated by the it reflected back to the aperture. Several works did measure the permittivity of low-loss materials [Chang et al., 1997, Tantot et al., 1997] such as Plexiglass using this method, however they did not discuss the boundary condition nor the size of sheet they measured.

With the choice made for the material under test, the testing setup must be assembled. The flange itself should be made from a 30 cm $\times$ 30 cm $\times$ 0.635 cm aluminum plate, milled to feature a 2.286 cm $\times$ 1.016 cm (0.900" $\times$ 0.400") hole (to mate with a WR-90 waveguide) along with holes to fasten the flange to the waveguide. The large size of the flange will allow for better correlation between the experimental data and the presented theory, allowing the approximation of an infinite flange in the theory to hold. The flange-waveguide assembly should be placed on top of the material under test, a 30 cm $\times$ 30 cm (0.635 cm and 1.270 cm thick) piece of absorbing foam (LS-10055 or LS-10211). The entire assembly should sit on a large metal plate approximating an infinite ground plane. With this test configuration, one should be able to collect data valid for comparison with the presented theory.

CHAPTER 3. Microstrip Sensor

The following chapter will cover the various aspects of the microstrip sensor solution proposed for non-destructive evaluation (NDE) of aircraft radomes. A brief overview of the various microstrip resonator geometries will be presented as well as a review of work previously done in applying microstrips resonators to NDE applications. It shall then cover the various steps taken in the design of the sensors. Finally, it will conclude with testing results over several test-pieces and provide analysis of the test results.

3.1 Introduction

As a key component in RF design, microstrip transmission lines and antennas are found in a variety of microwave applications. Consisting of a strip of metal on top of a dielectric substrate (backed by a ground plane), microstrips are small and lightweight, featuring a large bandwidth, and allow for miniaturization [Balanis, 1989]. These properties helped make microstrips a staple in microwave circuit design. However, when left unshielded, the simple design of the transmission line leaves it susceptible to interference with nearby circuitry and components [Balanis, 1989]. This seeming flaw of being sensitive to the transmission line's surroundings, coupled with the advantages listed above, make microstrips a viable candidate for use in a variety of nondestructive evaluation (NDE) applications. In particular, applications for determining layer thickness on a non-conductive substrate or examining composite structures would make ideal use of such a technology. The following chapter will provide an overview of the foundations of microstrip technology followed by a discussion of the application of microstrip-based NDE techniques to aircraft radomes.

3.1.1 Microstrips

Generally speaking, the basic structure of a microstrip follows that found in Figure 3.1. A thin strip of metal sits on top of a dielectric layer that is backed with a conductor. At sub-microwave frequencies (below ~300 MHz), the impedance of the transmission line may be approximated [Balanis, 1989] by

$$Z_0 = \begin{cases} \frac{60}{\sqrt{\epsilon_{\mathrm{r,eff,lt}}(0)}} \ln\left(\frac{8h}{w} + \frac{w}{4h}\right), & w/h \leq 1 \\ \frac{120\pi}{\sqrt{\epsilon_{\mathrm{r,eff,gt}}(0)}[w/h + 1.393 + 0.667\ln(w/h + 1.444)]}, & w/h > 1 \end{cases} \tag{3.1}$$

with the effective permittivities, $\epsilon_{\mathrm{r,eff,lt}}$ and $\epsilon_{\mathrm{r,eff,gt}}$, given as

$$\epsilon_{\mathrm{r,eff,lte}}(f=0) = \frac{\epsilon_r + 1}{2} + \frac{\epsilon_r - 1}{2}\left[\left(1 + 12\frac{h}{w}\right)^{-1/2} + 0.04\left(1 - \frac{w}{h}\right)^2\right] \tag{3.2}$$

$$\epsilon_{\mathrm{r,eff,gt}}(f=0) = \frac{\epsilon_r + 1}{2} + \frac{\epsilon_r - 1}{2}\left[1 + 12\frac{h}{w}\right]^{-1/2} \tag{3.3}$$

where the subscript lte indicates the value of $\epsilon_{\mathrm{r,eff}}$ when $w/h \leq 1$ and gt indicates $\epsilon_{\mathrm{r,eff}}$ when $w/h > 1$. When the frequency exceeds f_c as defined by [Balanis, 1989]

$$f_c = 0.3\sqrt{\frac{Z_c(0)}{h}\frac{1}{\sqrt{\epsilon_r - 1}}} \times 10^9 \tag{3.4}$$

where h is in centimeters, the strip is considered to be a dispersive transmission line, so a different set of equations must be used to model the transmission line [Balanis, 1989]:

$$Z_c(f) = Z_c(0)\sqrt{\frac{\epsilon_{\mathrm{r,eff}}(0)}{\epsilon_{\mathrm{r,eff}}(f)}} \tag{3.5}$$

$$v_p(f) = \frac{1}{\sqrt{\mu\epsilon_{\mathrm{eff}}(f)}} = \frac{v_0}{\sqrt{\mu_{\mathrm{r}}\epsilon_{\mathrm{r,eff}}(f)}} \tag{3.6}$$

$$\lambda_g(f) = \frac{v_p(f)}{f} \tag{3.7}$$

$$\epsilon_{\mathrm{r,eff}}(f) = \epsilon_r - \left[\frac{\epsilon_r - \epsilon_{\mathrm{r,eff}}(0)}{1 + \frac{\epsilon_{\mathrm{r,eff}}(0)}{\epsilon_r}\left(\frac{f}{f_t}\right)^2}\right] \tag{3.8}$$

$$f_t = \frac{Z_c(0)}{2\mu_0 h} \tag{3.9}$$

where v_p and λ_g are the phase velocity and group wavelength respectively. Additionally, $\epsilon_{\mathrm{r,eff}}(0)$ results from (3.2) or (3.3), depending on the ratio of w and h. It should be noted that the

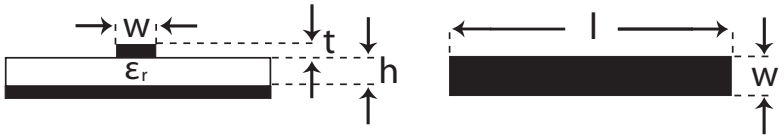

Figure 3.1 Schematic diagram of a microstrip transmission line.

metalization layer thickness t is very thin (less than 0.5 mm) and may be neglected when considering a series of layers.

On the theoretical side, Bahl and Stuchly [Bahl and Stuchly, 1980] developed an analytical approach (using the variational method) to explore the effect of covering a microstrip line with a sheet of dielectric material (both low and high-loss). This effect serves as the core principle utilized in the use of microstrips in NDE applications. By measuring the difference in behavior between a covered and uncovered microstrip, once may ascertain a variety of parameters of the sample under test. Details regarding this technique will be discussed in Section 3.2.

3.1.2 Coplanar Strip

In addition to the standard microstrip line, there exist many variations such as striplines and coupled microstrips. Coplanar strips (CPS), shown in Figure 3.2, compare quite closely to coupled microstrips (Figure 3.3), with both featuring two parallel strip lines situated on the same plane, except that the planar strips do not have a ground plane covering the back side of the dielectric (as illustrated in Figure 3.2). Analysis of these problems may take several forms - the quasi-static approach (good to approximately 8 GHz) and the fullwave approach [Gupta et al., 1979]. The quasi-static approach (e.g. conformal mapping) offers easier solutions but is approximate as it assumes the wave propagation to be pure TEM (transverse electromagnetic), while the fullwave approach (e.g. Galerkin's method) offers a more exact solution at the cost of greater complexity. From Gupta et al. [Gupta et al., 1979], the quasi-static formulation may be summarized as follows:

$$Z_{ocs} = \frac{30\pi}{\sqrt{\epsilon_{re}}} \frac{K(k)}{K'(k)} \tag{3.10}$$

$$k = \frac{S}{S + 2W} \tag{3.11}$$

where Z_{ocs} is the characteristic impedance of the CPS, ϵ_{re} is the effective dielectric constant experienced by the strip, and $K(k)$ is the elliptic integral of the first kind given by

$$K = \int_0^{\pi/2} \frac{d\theta}{\sqrt{1 - k^2 \sin^2 \theta}}. \tag{3.12}$$

K' is the derivitive of K given by

$$K' = \frac{dK}{dk} = \frac{E(k)}{k(1-k^2)} - \frac{K(k)}{k} \tag{3.13}$$

and $E(k)$ is the elliptic integral of the second kind.

$$E = \int_0^{\pi/2} \sqrt{1 - k^2 \sin^2 \theta} d\theta \tag{3.14}$$

The formulation for the integral ratios can be accurately and simply expressed [Gupta et al., 1979] by

$$\frac{K(k)}{K'(k)} = \frac{1}{\pi} \ln \left[2 \left(\frac{1 + \sqrt{k}}{1 - \sqrt{k}} \right) \right] \qquad \text{for } \tfrac{1}{\sqrt{2}} \le k \le 1 \tag{3.15}$$

$$\frac{K(k)}{K'(k)} = \frac{\pi}{\ln \left[2 \left(\frac{1+\sqrt{k'}}{1-\sqrt{k'}} \right) \right]} \qquad \text{for } 0 \le k \le \tfrac{1}{\sqrt{2}} \tag{3.16}$$

$$k' = \sqrt{1 - k^2} \tag{3.17}$$

and ϵ_{re} is obtained by the curve fitted equation

$$\begin{aligned} \epsilon_{re} \quad = \quad & \frac{\epsilon_r + 1}{2} \Big\{ \tanh \left[1.785 \log(h/W) + 1.75 \right] \\ & + \frac{kW}{h} \left[0.04 - 0.7k + 0.01(1 - 0.01\epsilon_r)(0.25 + k) \right] \Big\}. \end{aligned} \tag{3.18}$$

3.1.3 Coplanar Waveguide

The complement to the CPS is the coplanar waveguide, inverting the metal/non-metal areas (shown in Figure 3.4). Instead of having two parallel strips of metal, the CPS consists of a central strip with two ground planes on either side (parallel) located on the same plane [Gupta et al., 1979]. Since the two are complementary in their geometry, so too they are in

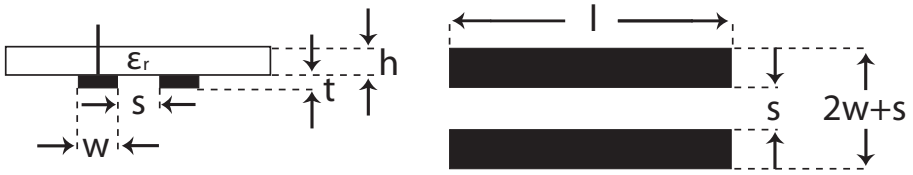

Figure 3.2 Schematic diagram of a coplanar strip (CPS) with a conductor tapping the resonaor through the substrate on the left strip. Side view presented at left, top view at right.

Figure 3.3 Schematic diagram of a coupled microstrip line. Side view presented at left, top view at right.

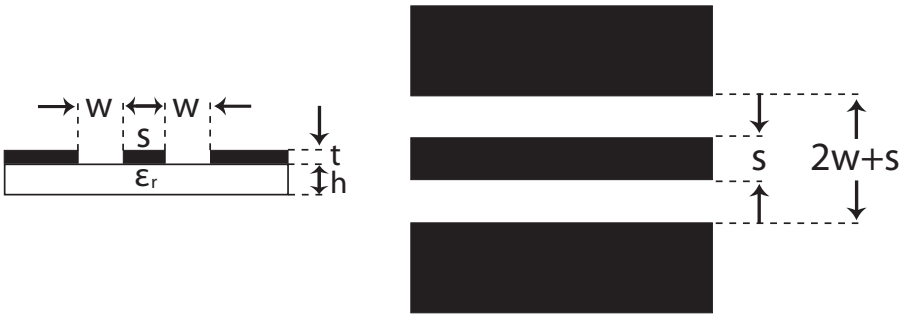

Figure 3.4 Schematic diagram of a coplanar waveguide (CPW). Side view presented at left, top view at right.

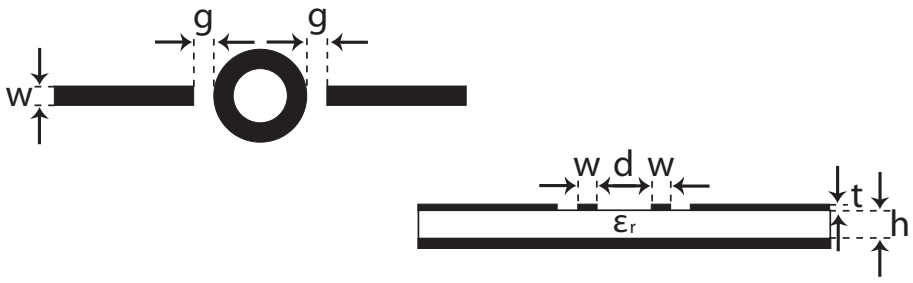

Figure 3.5 Schematic diagram of a ring resonator.

their formulation. From Gupta et al. [Gupta et al., 1979], the quasi-static formulation is as follows:

$$Z_{ocp} = \frac{120\pi}{\sqrt{\epsilon_{re}}} \frac{K'(k)}{K(k)} \tag{3.19}$$

where Z_{ocp} is the characteristic impedance of the of CPW, $K(k)$ is the elliptic integral of the first kind, and k is the ratio defined in (3.11). Z_{ocp} can be computed using (3.16) in place of the ratio of elliptic integrals.

3.2 Microstrip-based NDE Techniques

The vast majority of the early microstrip-based evaluation methods used a resonator constructed from a microstrip. The governing concept of the technique relies on changes to resonant frequency of the resonator due to the dielectric properties of the sample. The usage of microstrips to determine a material's dielectric constant started in the early 1970's with the work of Olyphant and Ball [Olyphant and Ball, 1970]. Work by Napoli and Hughes [Napoli and Hughes, 1971] utilized a different approach, measuring the resonant frequency of a dielectric covered (top and bottom) with a conductor (a microstrip line with its conductor sized the same as the ground plane) similar to that shown in Figure 3.5. Generally, however, these resonators took two forms: linear-shaped and ring-shaped. These will be described in the following two sections.

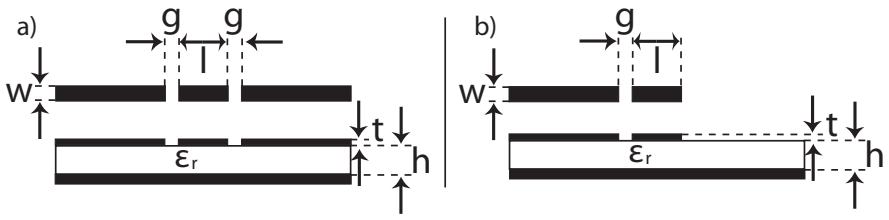

Figure 3.6 Schematic diagram of a) the transmission-based (two-port) linear resonator and b) the reflection-based (one-port) linear resonator.

3.2.1 Linear Resonator

Linear resonators feature a relatively straight-forward design, with a microstrip line coupling to a strip of a different width (typically 1/4 or 1/2 of a wavelength), then coupling on the opposite side to another line (of the same size as the feeding strip), shown in Figure 3.6. This structure resembles a filter. Olyphant and Ball used this configuration to obtain the measurements presented in [Olyphant and Ball, 1970]. Their efforts, as well as others [Itoh, 1974], aimed to determine the relative dielectric constant (ϵ_r) of substrates used for microwave integrated circuits.

Commonly, the resonant frequency and quality factor (Q, given by 3.20) were measured; from there, either ϵ_r was found directly, or it was obtained by finding an equivalent capacitance, then figuring the ϵ_r and loss tangent (δ). These applications were inherently destructive in nature because the resonator was deposited directly on to the substrate in question.

$$Q = \omega \times \frac{\text{Energy stored}}{\text{Power lost}} \tag{3.20}$$

3.2.2 Ring Resonator

Quite similar to the linear resonators described previously, ring resonators differ only in the geometry of the coupling element, shown in Figure 3.5. The first substantial non-destructive work examined moisture content in grains [Joshi et al., 1997]. For this application, a single grain of wheat was placed atop the ring, in line with the feed lines to the resonator. As with the linear resonator, the resonant frequency and the quality factor were the measured

parameters; this yielded a technique for moisture measurements with a resolution better than 1% [Joshi et al., 1997]. The change in resonant frequency due to the effective permittivity is shown by the following relation [Joshi et al., 1997]:

$$\frac{f_0^2}{f_s^2} = \frac{\epsilon_{\text{eff}_s}}{\epsilon_{\text{eff}_0}} \tag{3.21}$$

where the subscript s indicates when the sample is present and 0 indicates a free-space measurement. Similar work was performed by Sarabandi et al. [Sarabandi and Li, 1997] with using ring resonators to measure soil mosture. Later work by Abegaonkar et al. [Abegaonkar et al., 1999a] further explored measurements with wheat; [Abegaonkar et al., 1999b] studied the method on chickpeas with similar success. In a slightly different application, leaves were tested for their moisture content [Yogi et al., 1998].

Aside from agricultural applications, methods using a ring resonator were also applied to detect moisture content in paper. Yogi et al. [Yogi et al., 2002] fabricated a sensor on an alumina substrate, designed to operate at 10 GHz. This study, as well as those relating to the grain samples, were not concerned with spacial resolution, they were concerned with bulk-like measurements.

3.2.3 Microstrip Antennas

In contrast to the methods using the various transmission lines, techniques using microstrips to form antennas utilize a different approach. Microstrip antennas are quite commonplace in communications, found in various consumer electronics (e.g. mobile phones, handheld GPS units, etc.) as well as other applications. Foundational work by Bahl et al. [Bahl et al., 1982] explored the design considerations of microstrip antennas covered with a dielectric layer. As with the microstrips, the addition of the dielectric shifts the resonant frequency. The first-order change can be expressed by [Bahl et al., 1982]

$$\frac{\Delta f_r}{f_r} = \frac{\sqrt{\epsilon_e} - \sqrt{\epsilon_{e0}}}{\sqrt{\epsilon_{e0}}} \tag{3.22}$$

where f_r is the antenna's resonant frequency, Δf_r is the shift in the frequency, ϵ_{e0} is the uncovered effective permittivity, and ϵ_e is the covered effective permittivity.

Recently, work by Kim et al. [Kim et al., 2006] demonstrated a double-sided technique which utilized an array of microstrip patch antennas to measure the moisture in grains. This method measured the attenuation and phase-shift of the signal at the receiving end.

3.3 Coplanar Techniques

Relative to the microstrip linear resonator techniques, using a coplanar geometry for material characterization is new. For the most part, this technique also measures changes in the resonant frequency of a resonator due to the presence of a sample. As discussed in Sections 3.1.2 and 3.1.3, there are two complementary subgroups to this geometry: the coplanar strip (CPS) and coplanar waveguide (CPW). At present, only CPWs have seen any development for these applications, which shall be discussed below.

Use of the CPW for material characterization was first applied to dielectric film measurement as shown in Figure 3.7. Using a linear CPW resonator, Waldo et al. [Waldo et al., 1997] showed a variation in the resonant frequency due to the change in the thickness of a dielectric sample. As shown in Figure 3.8, the method shows a notable shift in frequency for a thickness up to 1.016 mm (40 mil), even for the lowest of the permittivities studied (3.27, the same as the CPW's substrate). As such, this technique seems ideal for measuring a thin coating of a low permittivity, such as a paint coating. The authors also point out that this may be adapted to the work of Root and Kauffman [Root and Kaufman, 1992], using the resonator as the frequency selecting component of an oscillator, thus eliminating the need for expensive microwave test equipment.

In designing the resonator, computer simulations were performed using commercially available software (Libra and em) to determine optimal dimensions. Figure 3.7 shows the general design of the structure. The simulations generally matched the measured data. The authors attributed the measurement error to approximations in the simulation, thin air gaps between the strips and the top layer in the experimental setup, and the tolerances for fabrication.

In another study, a half-wavelength linear resonator was constructed on an alumina ($\epsilon_r = 9.8$) substrate [Demenicis et al., 2007]. This resonator, however, utilized a two-port design

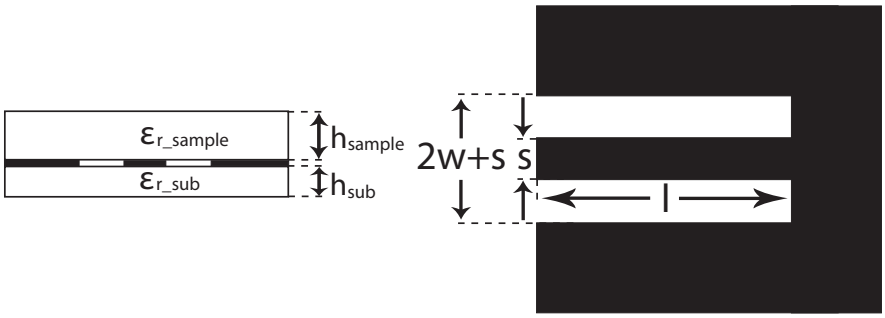

Figure 3.7 Schematic diagram of the reflection-based (one-port) CPW resonator used by Waldo [Waldo et al., 1997].

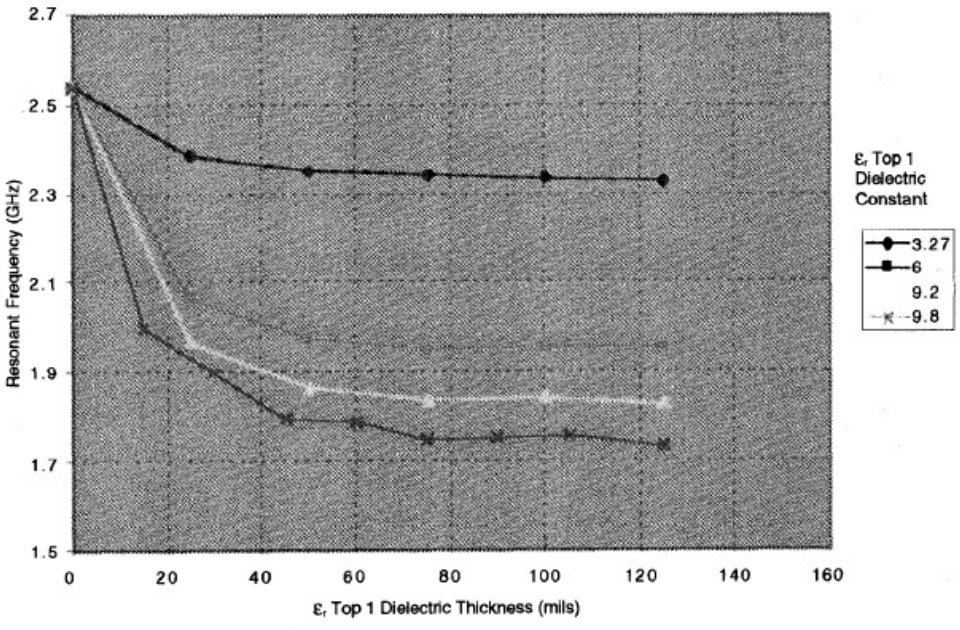

Figure 3.8 Measured resonant frequency vs. top dielectric thickness for a substrate dielectric constant of 3.27, 6.0, 9.2, and 9.8 [Waldo et al., 1997].

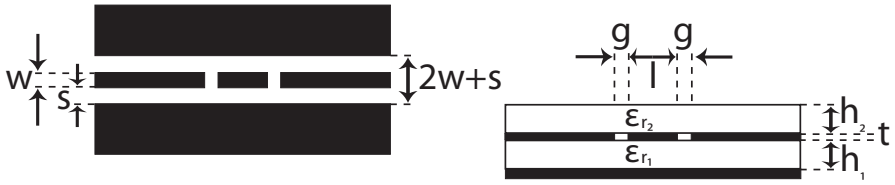

Figure 3.9 Schematic diagram of the transmission-based (two-port) CPW resonator used by Demenicis [Demenicis et al., 2007].

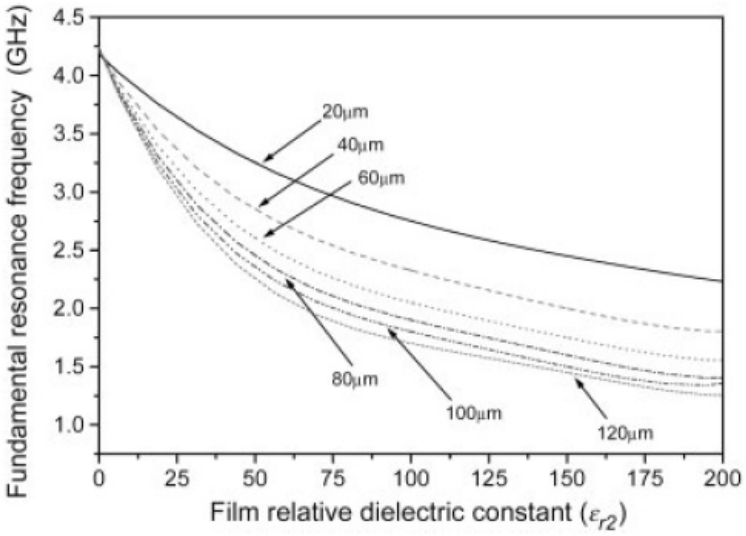

Figure 3.10 Theoretical prediction for the resonant frequency based on the film dielectric constant using a two-port CPW linear resonator [Demenicis et al., 2007].

(see Figure 3.9), instead of the single-port in [Waldo et al., 1997]. As such, the S_{21} scattering parameter (S-parameter) was the measured quantity. The free-space (un-loaded) resonant frequency was designed to be 4.15 GHz, and varies as shown in Figure 3.10.

Work by Hu et al. utilized a grounded CPW to determine both permittivity and permeability of an unknown material [Hu et al., 2006]. A ground plane was attached to the bottom of the substrate material and to the top of the sample material. Extracting these parameters requires the calculation of filling factors using conformal mapping. When the filling factors are used with the duality property, the effective permittivity and permeability of the entire structure (and that of the unknown sample) can be determined by deriving a relationship with the characteristic impedance and the structure's propagation constant (γ, obtainable from the

measured S-parameters). These filling factors, q_1 and q_2, are computed with the following equations [Hu et al., 2006]:

$$q_1 = \frac{\frac{K(k_1)}{K(k_1')}}{\frac{K(k_1)}{K(k_1')} + \frac{K(k_2)}{K(k_2')}} \tag{3.23}$$

$$q_2 = \frac{\frac{K(k_2)}{K(k_2')}}{\frac{K(k_1)}{K(k_1')} + \frac{K(k_2)}{K(k_2')}} \tag{3.24}$$

where $K(k)$ is an elliptic integral of the first kind and k by [Ghione and Naldi, 1987], [Bedair and Wolff, 1992]

$$k_1 = \tanh\left(\frac{\pi w}{4h_1}\right) / \tanh\left(\frac{\pi(2s+w)}{4h_1}\right) \tag{3.25}$$

$$k_1' = \sqrt{1-k_1^2} \tag{3.26}$$

$$k_2 = \tanh\left(\frac{\pi w}{4h_2}\right) / \tanh\left(\frac{\pi(2s+w)}{4h_2}\right) \tag{3.27}$$

$$k_2' = \sqrt{1-k_2^2}. \tag{3.28}$$

The computed values for q_1 and q_2 may then be used in the

$$\epsilon_{r2} = \frac{\epsilon_{\text{reff}}}{q_2} - \frac{q_1\epsilon_{r1}}{q_2} \tag{3.29}$$

$$\mu_{r2} = \frac{q_2\mu_{r1}\mu_{\text{reff}}}{q_1}\left(\frac{\mu_{r1}}{q_1} - \mu_{\text{reff}}\right)^{-1} \tag{3.30}$$

where the effective permeability and permittivity is a ratio of the transmission line's capacitance fully loaded ($Z_{\text{c\_loaded}}$) to the capacitance of the line without any dielectric present ($Z_{\text{c\_free}}$) [Hu et al., 2006], and calculated by [Carlsson and Gevorgian, 1999], [Matthaei et al., 1990]

$$\epsilon_{\text{reff}} = \frac{Z_{\text{c\_loaded}}\gamma}{\omega Z_{\text{c\_free}}\sqrt{\epsilon_0\mu_0}} \tag{3.31}$$

$$\mu_{\text{reff}} = \frac{Z_{\text{c\_free}}\gamma}{\omega Z_{\text{c\_loaded}}\sqrt{\epsilon_0\mu_0}}. \tag{3.32}$$

The results from this method were accurate to within 2% between 5 and 15 GHz.

3.4 Coplanar Stripline Design and Simulation

The design process for the coplanar stripline used in this research progressed primarily as an iterative process. The length of the quarter-wavelength resonator was chosen to be 10.93

mm. This value was computed with a design frequency of 4 GHz and a substrate dielectric constant of 2.94 (Rogers 6002 RF laminate) using the approximation given by Equation 3.33. This equation is an approximation since it actually computes the wavelength inside a block of the laminate material, not on a finite layer (surrounded by free-space) as manifested by the sensor. The width (w) and strip separation (s) were then 'fine-tuned' to achieve the best sensitivity.

$$l \approx \frac{1}{4}\lambda = \frac{1}{4}\frac{c}{f} = \frac{1}{4}\frac{1}{f\sqrt{\epsilon_0 \epsilon_r \mu}} \tag{3.33}$$

Prior to fabrication, the effect of the sensor substrate's permittivity on the size of the resonance shift was studied using computer simulations. To this end, Agilent's ADS Momentum software package provided the simulation environment. Three substrates were considered: Rogers 6002, Isola FR408, and FR4. The first two materials, with ϵ_r equal to 2.94 and 3.63 respectively, are RF laminate materials designed for use as circuit boards in high performance RF applications; FR4 ($\epsilon_r = 4.31$) is standard circuit board material. The advantage to the RF laminates lies in their consistent electrical behavior over the range of frequencies under this examination. Additionally, they exhibit a much lower degree of loss/dispersion compared to FR4, allowing the sensor to be more sensitive to the dielectric features in the test-piece. However, this grade of performance comes at a high price due to both the cost of material and the processing difficulty associated with circuit fabrication on the material. Conversely, FR4 is quite common so it very low cost, but its dielectric behavior is not consistent in the microwave regime, exhibiting some dispersion and attenuation due to loss in the dielectric, thus it's generally avoided in most microwave applications. In this study it was elected to use FR4 for preliminary measurements.

For each strip/substrate configuration, several simulations were performed. The first set examined an "uncovered" resonator (no layer atop the stripline), one covered by a 1.473 mm (58 mil) sheet of quartz[1] ($\epsilon_r = 3.78$ [Press, 2004]) sheet on top, a 1.524 mm (60 mil) quartz layer, and finally a 1.575 mm (62 mil) quartz layer.

From there, the resonant frequency (obtained from the minimum peak value of the S_{11}

[1]The choice for quartz arose from the fact many radomes use facesheets of quartz fiber reinforced composite.

scattering parameter) of each layered simulation was subtracted from that for the uncovered resonator; this yields the shift in resonant frequency Δf. A plot of the results for each resonator are shown in Figure 3.11. A similar exercise was performed for a Rexolite® test-piece ($\epsilon_r = 2.53$ from 0-500 GHz [C-LEC Plastics, 2008]), shown in Figure 3.12. These two results are compared against one another for the case of the 1.524 mm top-layer in Figure 3.13.

As one may note in examining the results of these simulations, the Rogers 6002 substrate material exhibits the greatest $|\Delta f|$, thus making it the best performing. However, although it exceeds the two other materials in performance, its margin is small. All three materials resonated between 3.8 and 5 GHz, depending on the testing configuration. Even FR4, the weakest of the three, still manages a shift of 0.9 GHz for the quartz sample (compared to the 1.2 GHz found with Rogers 6002). It also should be noted the size of the strip width and spacing between the strip did not seem to make a big difference in the results. Considering the cost of the laminates as well as the difficulty/cost associated with fabrication, coupled with the laminate's "negligible" gain in performance, FR4 was chosen for the substrate of the sensors.

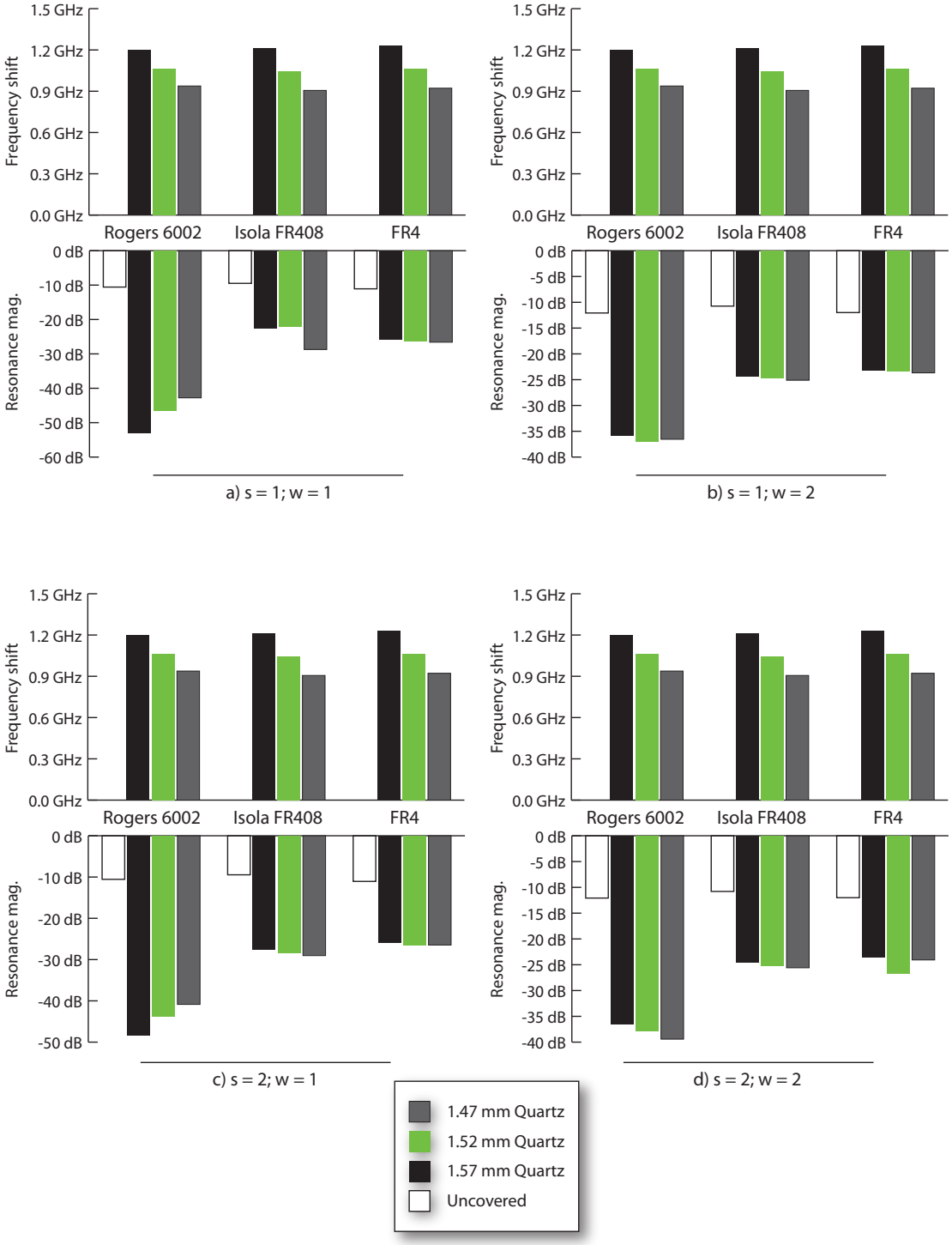

Figure 3.11 Simulation results for the resonant frequency shift (Δf) and magnitude for three quartz ($\epsilon_r = 3.78$ [Press, 2004]) top-layer samples and an uncovered stripline for (a) $s = 1$ and $w = 1$, (b) $s = 1$ and $w = 2$, (c) $s = 2$ and $w = 1$, and (d) $s = 2$ and $w = 2$ (all dimensions in mm, see Figure 3.2).

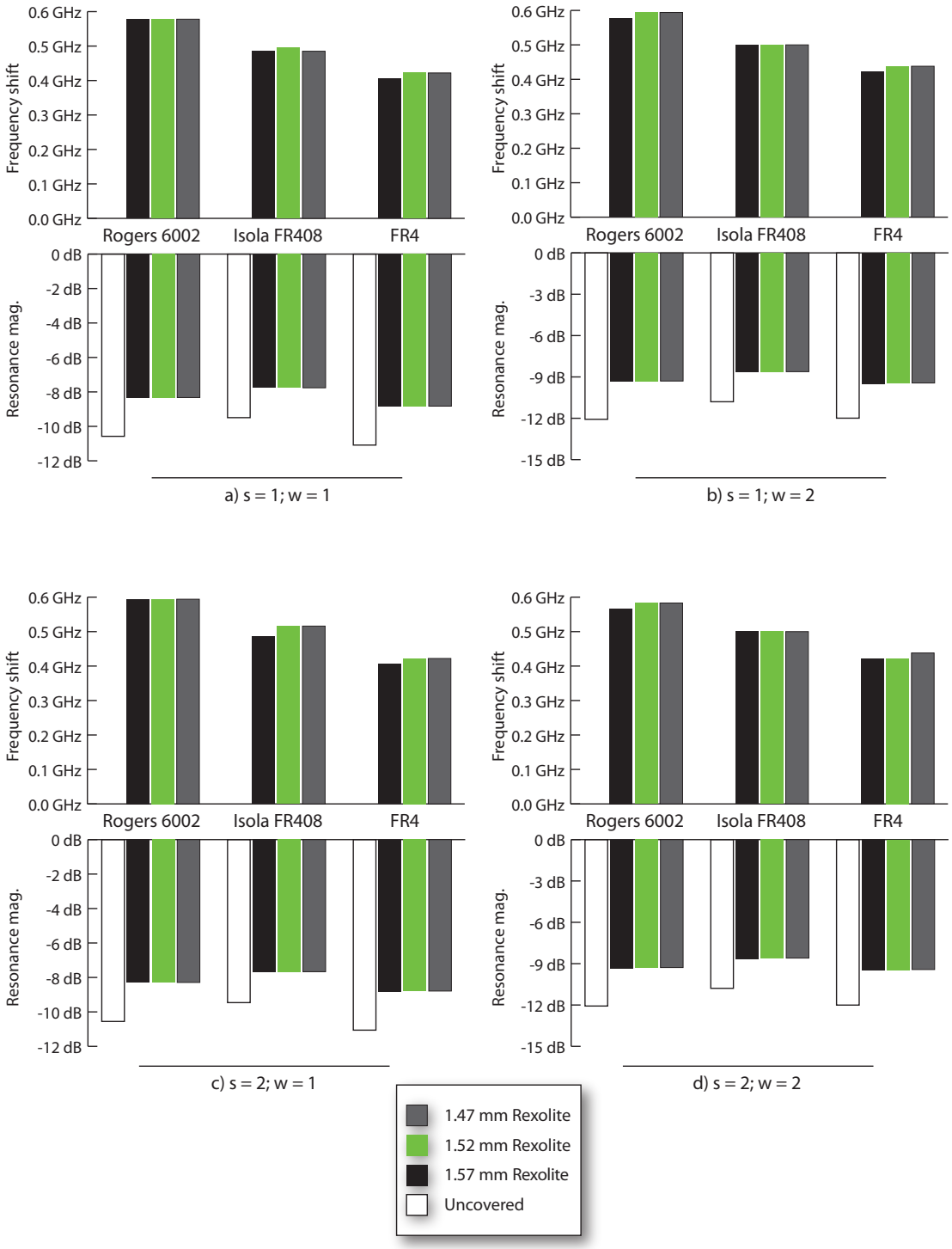

Figure 3.12 Simulation results for the resonant frequency shift (Δf) and magnitude for three Rexolite® ($\epsilon_r = 2.53$ [C-LEC Plastics, 2008]) top-layer samples for (a) $s = 1$ and $w = 1$, (b) $s = 1$ and $w = 2$, (c) $s = 2$ and $w = 1$, and (d) $s = 2$ and $w = 2$ (all dimensions in mm, see Figure 3.2).

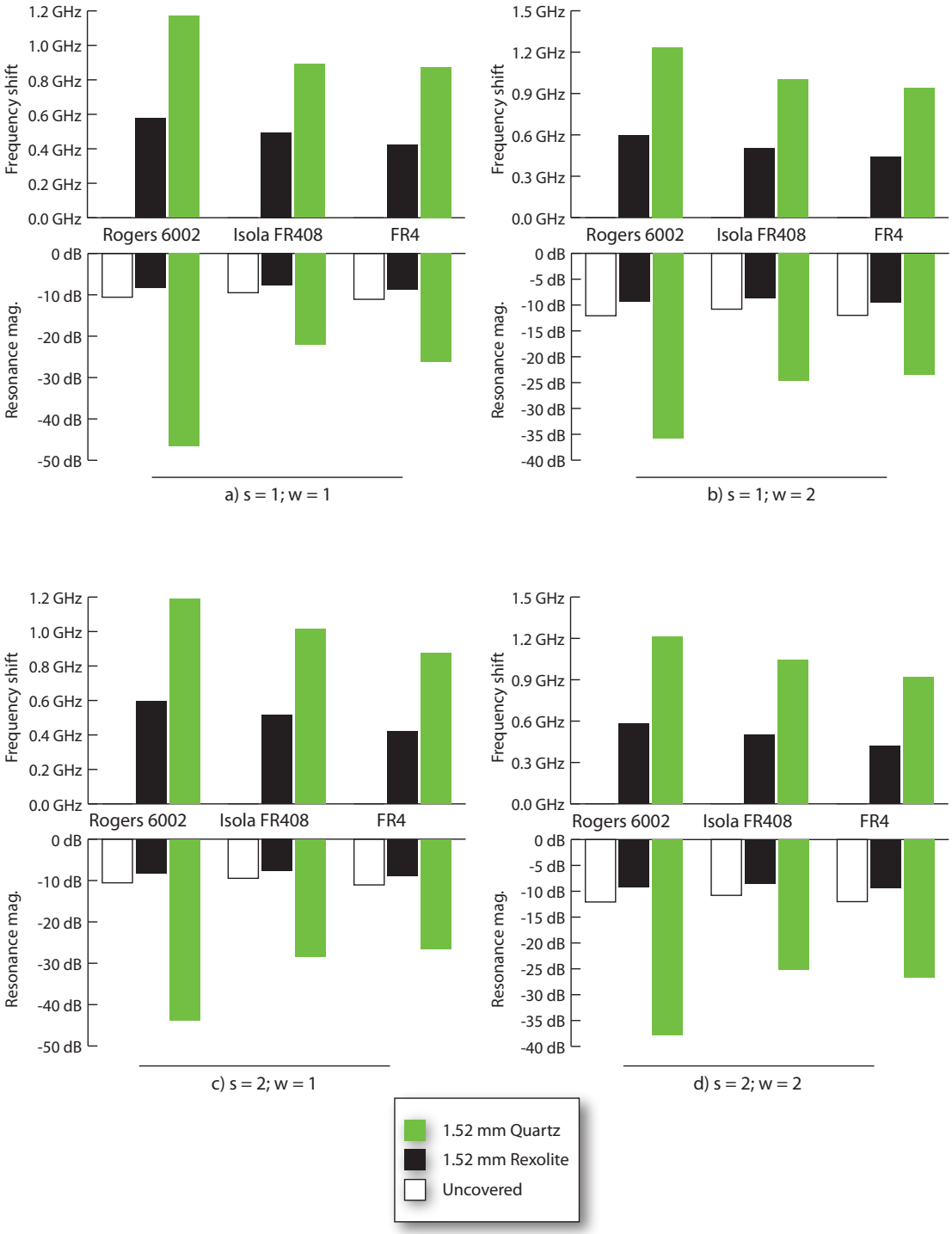

Figure 3.13 Simulation results for the resonant frequency shift (Δf) and magnitude for three substrate configurations (uncovered, 1.52 mm quartz, 1.52 mm Rexolite®) for (a) $s = 1$ and $w = 1$, (b) $s = 1$ and $w = 2$, (c) $s = 2$ and $w = 1$, and (d) $s = 2$ and $w = 2$ (all dimensions in mm, see Figure 3.2).

Sensor type	Strip width (w)	Strip separation (s)	Strip length (l)
A	1 mm	1 mm	10.93 mm
B	1 mm	1 mm	10.93 mm
C	1 mm	1 mm	10.93 mm
D	2 mm	2 mm	10.93 mm

Table 3.1 Listing of fabricated sensor dimensions for the coplanar stripline resonator.

3.5 Coplanar Testing

As a proof of concept, the board layout was fabricated on standard FR4 material. FR4 has the distinct advantage of being commercially fabricated at significantly lower cost, with respect to both the material as well as the ensuing cost of manufacturing, compared to the RF laminates. Unfortunately, the material bears a significantly larger permittivity in the microwave regime compared to the RF laminates (4.31 compared to 2.94 and 3.63 for Rogers 6002 and Isola FR408 respectively). Additionally, the loss tangent for FR4 becomes significant in the microwave range (greater than 0.01), dampening the resonant effects of the stripline, where as the loss tangent for the laminates remains negligible. By increasing the permittivity of the sensor's substrate, the resonator becomes less sensitive to changes in the test-piece's permittivity (and therefore its ability to sense water ingression or other permittivity changes). This was evident from the simulations made using Agilent's ADS Momentum presented in Figure 3.13. Despite it showing the weakest performance in the simulations, the 0.9 GHz shift exhibited in the quartz layer simulations still demonstrated FR4 to be potentially capable as a substrate for the sensor.

3.5.1 Initial testing

Accordingly, FR4 was chosen for "proof of concept" testing. Four variations were fabricated by an outside vendor (Advanced Circuits), shown in Figure 3.14; the corresponding dimensions are shown in Table 3.1.

For initial testing, the D-type sensor was selected. A via was drilled through the backside of the circuit board 1/4 of the strip length (2.7 mm) away from the edge of one of the strips. The

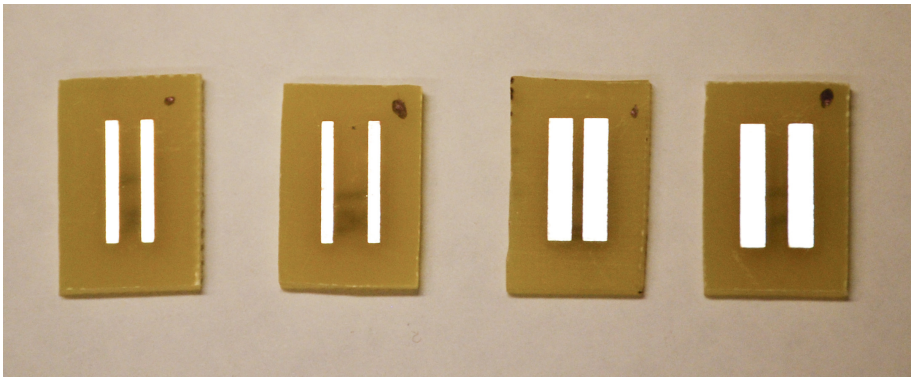

Figure 3.14 Fabricated CPS resonator sensors, order A through D (left to right).

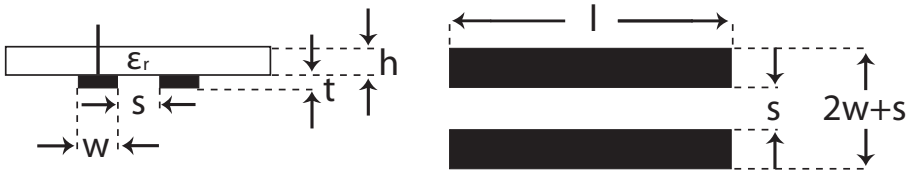

Figure 3.15 Schematic of wired coplanar stripline sensor.

depth went down to the edge of the metal layer, however it did not puncture. From there, the central conductor of an SMA connector was placed through the hole to directly connect it to the strip. A schematical representation is shown in Figure 3.15. The electrical connection between the connector's central conductor and the strip metalization was made through forced contact; it was not soldered as the proper equipment for soldering a microwave-quality connection was not available. 'Hot glue' was deposited around the edge of the conductor to afix the connector to the sensor. This assembly was mounted in a PVC fixture to provide a robust aparatus to hold the sensor during testing, shown in Figure 3.16.

For testing, the fabricated sensor assembly was mounted statically above a simulated radome sandwich structure. This consisted of two 2.38 mm (3/32") sheets of Rexolite® ($\epsilon_r = 2.53$) separated by 6.35 mm (0.25"). This separation was chosen because an obtained radome sample had a separation between the skins of roughly a quarter inch (details of the radome sample may be found in Table 3.3). A ceramic alumina "defect" ($\epsilon_r = 8.5$) was introduced between the layers, dimensioned 6.35 mm × 6.35 mm × 25.4 mm (0.25" × 0.25" ×

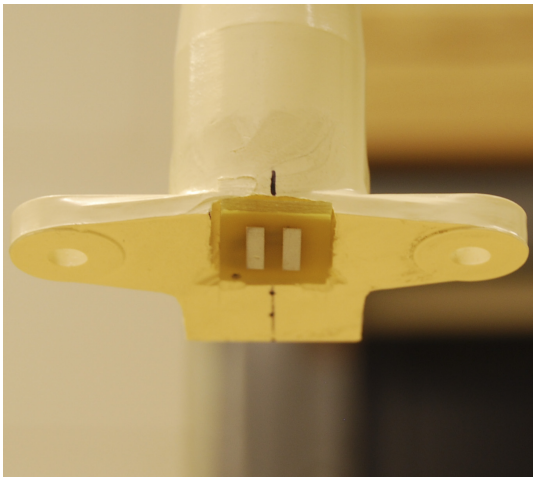

Figure 3.16 D-type coplanar stripline sensor mounted in PVC fixture.

1.0"). The alumina served as a fair "middle of the road" defect, as its permittivity is higher than that of excess paint or resin however it's considerably lower than water. This structure was placed on top of a Plexiglass® platform (shown in Figure 3.17) to distance it from any local dielectric anomalies present in the testing setup.

Prior to testing, the vector network analyzer (VNA) requires calibration to de-embed (remove the effects of) the cable and test-ports on the test equipment. The calibration procedure is done through a 3-stage process. First, an open-circuit is put on the end of the cable, consisting of an SMA connector with a copper waveguide soldered around the edge (connected to the outer conductor). Next, a short is put on the end of the cable, formed with an SMA connector which has a piece of copper soldered to both the central conductor as well as the outer conductor. Finally, a 50Ω broadband load is placed on the end of the cable for the last stage. This procedure is best performed after the VNA has been powered on for several hours.

With the VNA calibrated, the testing may begin. The scan was performed over a 25.4 mm × 50.8 mm (1" × 2") area scanned at increments of 2.54 mm (0.1"). At each point, the S_{11} parameter was measured on the VNA and the resonant frequency and the magnitude of S_{11} were recorded. A schematic of the area, as well as the measured resonant frequencies, are shown in Figure 3.18. As one may note, the defect shows up quite clearly in the image. The average resonant frequency of the non-defective area is 8 GHz; conversely the average resonant

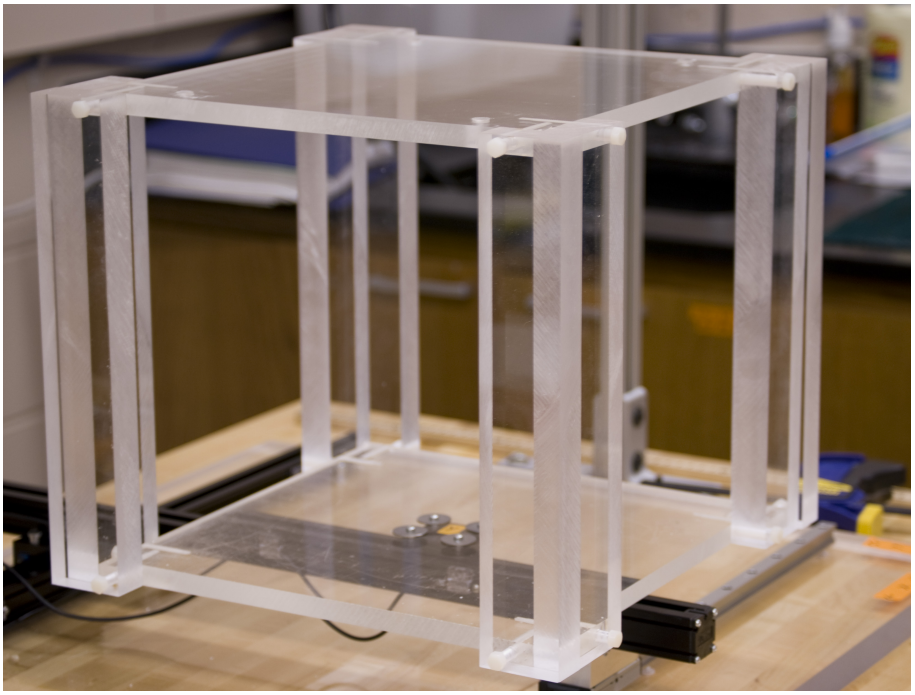

Figure 3.17 Plexiglass platform for measurement isolation, mounted on an X-Y positioning stage.

frequency for the defective area is 3.48 GHz. This produced a net shift of 3.52 GHz. From the perspective of an inspection, this indisputably represents an anomaly in the structure.

The standard used above for measuring the resonant frequency looked for the largest magnitude on the reflection coefficient. This peak magnitude is actually the smallest value of the reflection coefficient (since it's measured in dB), which signifies the point of least reflection back to the network analyzer. One way of looking at this is to see the resonator acting as a 'matched load' to cable/VNA. The resonance is the point of maximum energy transfer to the resonator.

By this measurement criteria, the shift discussed above was not actually a shift in a peak, but a 'trading' of a resonant peak. Over the defective area, the 8 GHz peak shrank in magnitude while the 3.48 GHz peak increased. More of this phenomena will be discussed in Section 3.5.2. It should be noted that due to the asymmetry of the probe, a rotation of 90° would yield slightly different results. In a commercial setting, this could be compensated with re-computing the coordinate system. This could also be adjusted with a sensor calibration step.

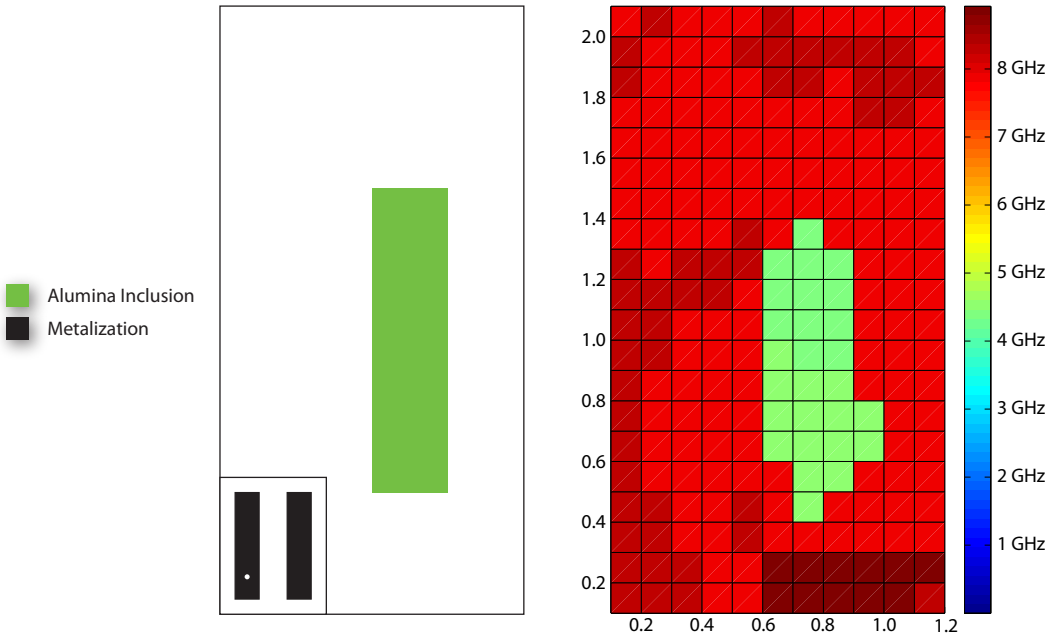

Figure 3.18 A schematic of the layout (to scale) for initial Rexolite®/alumina test-piece (left). The black strips in the lower left display the relative size of the sensor, where the white dot on the left sensor indicates the tapping point for the connector. Right, a plot of the measured resonant frequency obtained from the scan (units are in inches).

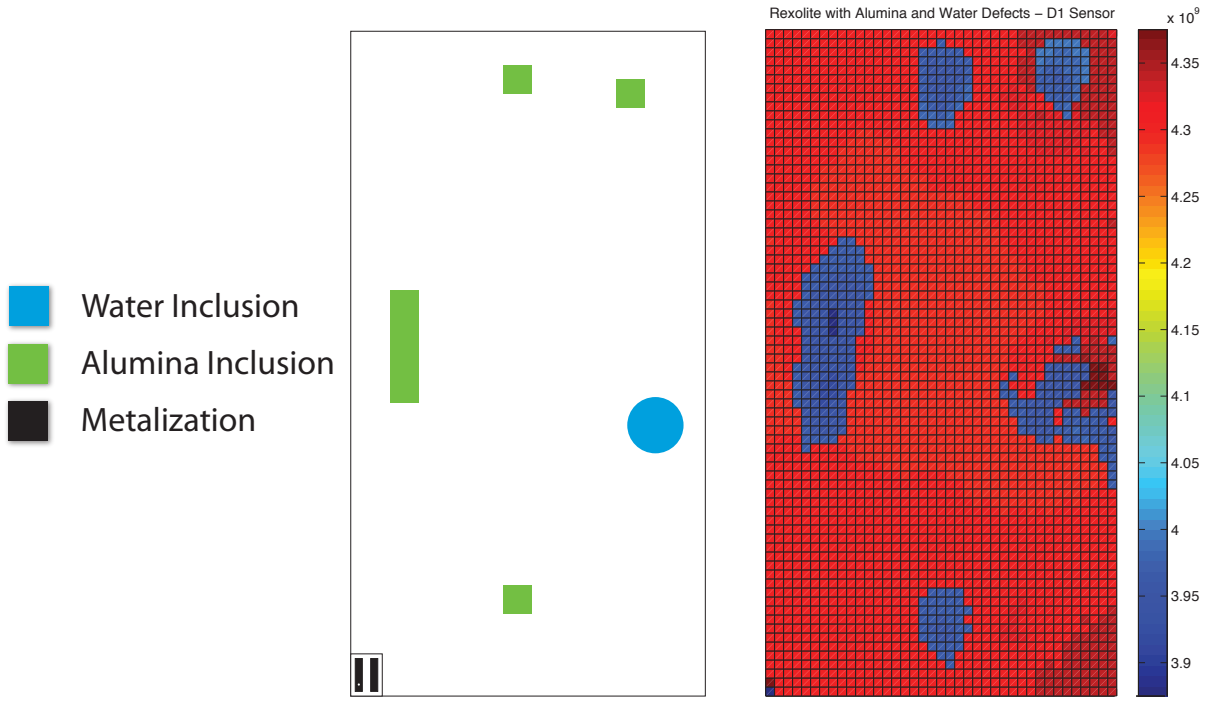

Figure 3.19 Schematic of the Rexolite®/alumina/water testing configuration, to scale (left), and a plot of the resonant frequency measured during the scan (right). The black strips in the lower left display the relative size of the sensor, where the white dot on the left sensor indicates the tapping point for the connector.

3.5.2 Wide-area testing

To assess the performance of the sensor over a larger area, a test piece was constructed in a similar manner to that of the initial scan. The 2.38 mm (3/32") thick Rexolite® sheets were assembled 6.25 mm (0.25") apart with the 25.4 mm (1") piece of alumina from the first test, several 6.35 mm (0.25") cubes of alumina, and 0.5 cc of water placed in a plastic container with a diameter of 19.05 mm (0.75"), height of 6.25 mm (0.25"). A comprehensive list of the permittivities of the materials used in this test may be found in Table 3.2. An automated scan was performed over an 8 cm × 16 cm area incremented with a step size of 2 mm. The results are shown in Figure 3.19.

As with the initial scan, the results are generated on the basis the 'trading' of a resonance

Material	ϵ_r(4 GHz)
Air	1
Rexolite®	2.53
Ceramic alumina	8.5
Water	75.3 - j14.6
FR4 (sensor substrate)	4.31 - j0.07

Table 3.2 List of dielectric constants at 4 GHz for the materials found in the wide-area scan.

peak. The plots in Figure 3.20 show S_{11} (reflection coefficient) over a defective area and non-defective area. The measured frequency shift in both this wide-area scan, as well as the initial scan, occurred as a result of a trading between the multiple resonances shown in Figure 3.20. Over the defect, the magnitude of the peak at 3.95 GHz was the greatest while elsewhere the 4.40 GHz peak proved strongest. The reason for these two peaks most likely results from parasitics capacitances/inductances present from something such as the connection between the connector and the strips. It should be noted a shift of the 4.40 GHz peak did occur (as noted in Figure 3.20), however it amounted to less than 0.1 GHz.

The peak-trading in the initial test occurred between two different peaks, one at 8 GHz peak shrank in magnitude while the 3.48 GHz. The peak at 8 GHz is a half-wavelength resonance, which is also present in the wide-area scan as shown in Figure 3.20. Between these two tests, the connector on the sensor required removal and replacement on the sensor, affirming the suspicion the various resonances are related to issues with the connection between the connector and the strip.

Despite the difference in the peak-trading behavior, the 'shift' still stands out. The resultant image (Figure 3.19), as a whole, represents the test-piece layout with a strong correspondence to the schematic. The 25.4 mm (1") alumina defect shows up at a slight angle compared to the schematic; however, after further investigation of the test setup, the alumina was found to have shifted from its original placement in a manner reflecting that in the image. The sizes of the defects depicted in the image appear larger than the defect itself; the defects even affected the resonance with only a partial coverage of the sensor.

The one area of the image that does not correspond well with the diagram is the water

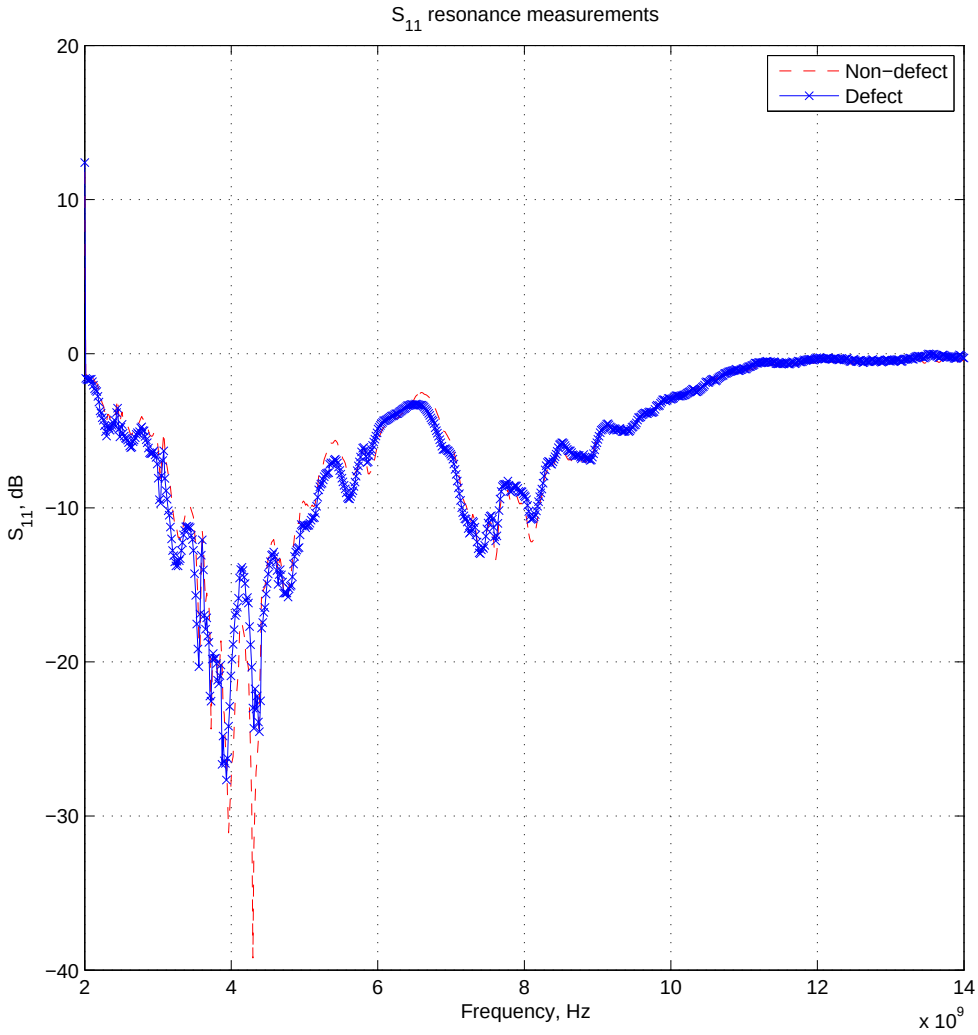

Figure 3.20 Plot of the measred S_{11} for the sensor over an alumina defect ($\epsilon_r = 8.5$) and a non-defective area from the Rexolite®/alumina/water test, shown in Figure 3.19.

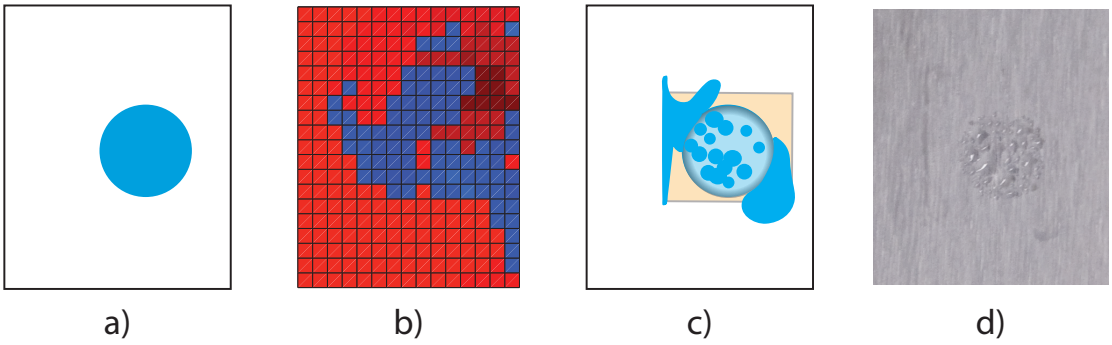

Figure 3.21 a) The intended water defect in the wide-area scan. b) Resultant image generated from the scan. c) Schematic of actual water defect area. Deep blue regions indicate water on underside of top Rexolite® layer; the light blue represents the remaining water in the container. The light yellow represents the plastic lip of the water container that interfaced with the top layer. d) Picture of water condensation on underside of top Rexolite® layer (image mirrored to match top views in this figure).

defect. As shown in detail in Figure 3.21, the defect seems to conglomerate in the area around the intended location of the water, with a partial void formed around actual placement of the water. Several factors impacted this finding. Upon disassembly, the water level in the container was found lower than the original level. Some water had evaporated and condensed on the top Rexolite® layer. Other water became lodged between the top plastic lip (shown as the light yellow region in Figure 3.21c) that surrounded the outer perimeter of the container and the top layer. The Rexolite® seemed somewhat hydrophilic, partially influenced by the grain molded into the plastic, noticeable in Figure 3.21d. These small channels allowed for water caught between the top layer and the lip of the water container to migrate beyond this interface (as represented in Figure 3.21c). Additionally, the water remaining in the container formed a meniscus along the outer edge, shown by the darkened edge around the circle in Figure 3.21c.

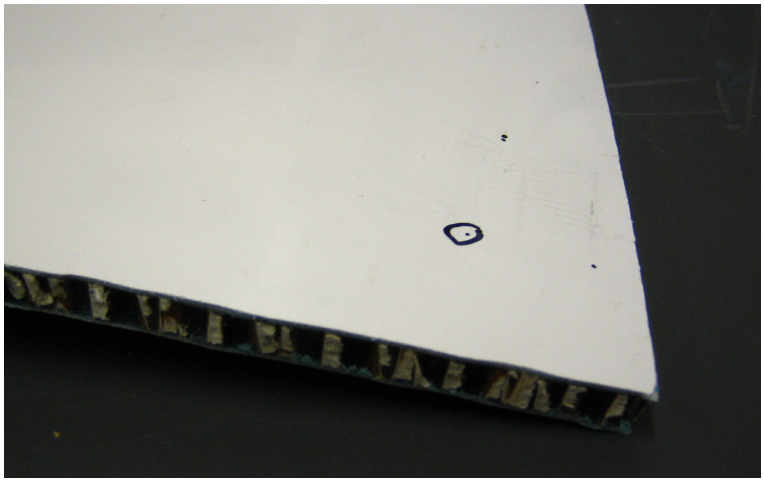

Figure 3.22 Saint Gobain radome sample with introduced water ingression. The water was injected using a hypodermic needle through the side at the black circled point on the top layer.

Parameter	Value
Total thickness	0.370”
Core thickness	0.290”
Inner skin thickness	0.035”
Outer skin thickness (painted)	0.045”
Cell volume	0.2 cc

Table 3.3 Properties of the Saint Gobain radome sample [Hsu, 2007] All values are within 0.005”.

3.5.3 Radome testing

For a final proof of concept test, the sensor was applied to detect water ingression inside a sample radome provided by Saint Gobain, shown in Figure 3.22. For this experiment, 1 cc of water was injected using a hypodermic needle into a portion of a honeycomb core radome. Detailed information about the radome test-piece may be found in Table 3.3. With the honeycomb cells each having a volume of 0.2 cc, the ingression occupied up to 5 cells.

Due to the curvature of the radome, a hand spot test was performed rather than an automated X-Y scan. The probe (recessed in the PVC fixture) was placed over a non-defective area and the resonant frequency was measured, listed in Table 3.4. This yielded a resonance of 4.18 GHz. The probe was then moved over the region with the water ingression. The resonant frequency shifted to 3.95 GHz. This series of measurements was repeated, varying the

Parameter	Value
f_{defect}	3.95 GHz
f_{normal}	4.18 GHz
Δf	0.23 GHz

Table 3.4 Results for radome spot test.

non-defective inspection location; the results remained the same, netting a 0.23 GHz shift. It should be noted that in this test, the change in the resonant frequency occurred due to an actual shift in frequency and not a 'trading' on frequency peaks.

3.6 Coplanar Testing Assessment

As a whole, the coplanar stripline resonator technique detected and located the defects repeatably. The images produced showed the location of the defects quite well and would be easily noted during an inspection. Although the shift in resonant frequency did not occur precisely as theorized, the system still yielded useful results from the scans. The underlying theory for this technique approximately follows Equation 3.34, where λ remains constant (being related to four times the length of the resonator), and $\epsilon_{\text{eff}}/\mu_{\text{eff}}$ change with the depending on the material below the metalization (circuit board substrate) and the material above (test-piece). The larger the effective permittivity, the lower the resonant frequency will be. It should be noted that Equation 3.34 assumes the entire medium surrounding the material is one particular material of infinite size. It also does not take into account how the resonator is connected. Despite these assumptions, it provides an approximate result which is supported by the Agilent ADS simulations (presented in Section 3.4). When the test-piece was added, the simulations showed a lowering of the resonant frequency by approximately 1 GHz.

$$\lambda f = c = \frac{1}{\sqrt{\epsilon_{\text{eff}}\mu_{\text{eff}}}} \tag{3.34}$$

The results gathered from the wide-area scan seemed to correspond approximately to the simulation results in that the overall resonant frequency was in the same range as the simulation. However, in this particular implementation, multiple quarter-wavelength resonances appeared. The reason for the occurrence of the multiple resonances is multifold. The two res-

onances at 3.95 and 4.4 GHz in Figure 3.20 are quarter-wavelength resonances, supported by their correspondance to both the approximate values computed using Equation 3.34 and the ADS simulations. The fact there are two quarter-wavelength resonances may be attributed to the parasitic capacitances/inductances introduced between the connector's central conductor and the stripline. Additional resonances found between 7 and 9 GHz are the half-wavelength multiples of the quarter-wavelength resonances.

The trading of the resonance peak might offer yet another technique for sensing, one which is less susceptible to noise from the probe itself, removing an element of uncertainty. A very small shift (less than 0.1 GHz) in resonant frequency could be hard to note in measurements and become introduced by a slight change in the angle of the probe's interface with the test-piece (tilt). Conversely, if the peak-trading pheomena is utilized, the peak trade might still occur over a defect even with the introduction of probe tilt, which would make this an ideal technique for field use.

3.7 Further Work

There remains much to investigate regarding this technique. Among these different items, further assessment of the probe's parameters ranks highest. Testing of different configurations such as the other sensor types fabricated to analyze the effects of variations in the strip width (w), strip separation (s) as well as the point on the strip where the conductor interfaces the connector would yield an optimized design, potentially more sensitive to changes in the sample.

Another area of inquiry deals with the sensors sensing capabilities. The feature resolution as well as the smallest detectable feature size should be investigated. Both water and alumina were tested as defects, however further testing using defects of low permittivity (such as resin or Rexolite®) would better prove the system's ability to detect more subtle variations in the radome. Also, the effective sensing penetration depth should be investigated. To this end, testing should be done varying the gap between the defect and the top layer.

Aside from the defect-layer gap, the effect of probe lift-off, the gap between the test-piece and the probe, should also be investigated further. Preliminary findings based on setup of

the conducted tests seem to indicate the probe does have some notable sensitivity to lift off. Because this technique relies on near-field interactions, it would not be a surprise that its sensitivity would drop significantly as the distance between the probe and the top of the test-piece increases. This characteristic needs to be investigated further, particularly in the context of how changes in the probe's geometry change the lift-off sensitivity.

Finally, investigation of different resonator geometries could potentially yield better sensitivity and resolution. Architectures such as the coplanar waveguide (used in [Waldo et al., 1997, Hu et al., 2006, Demenicis et al., 2007]) or a ring resonator (previously implemented in [Joshi et al., 1997, Abegaonkar et al., 1999a, Yogi et al., 1998]) offer a variety of distinct field configurations. These differences could prove especially sensitive for a particular type/shape of defect (for example, one type of resonator may prove ideal for sensing paint thickness on a curved surface).

CHAPTER 4. Conclusion

The work presented in this thesis sought to investigate a microwave NDE technique to investigate aircraft radomes. With the radar's high sensitivity to variations in the radome's dielectric constant, there exists a need for a technique that can detect defects such as water ingression and paint layer thickness. The only widely used technique that assesses for these dielectric anomalies, a transmission test, is cumbersome to perform, requiring the radome to be removed from the aircraft and brought to a special lab for testing. Accordingly, a new microwave-based technique was proposed to fill this inspection deficiency.

The first technique considered was an open-ended rectangular waveguide. Applied in a variety of different applications, this method is relatively mature in its characterization. Relying on reflection of microwave energy off the test-piece, the inspector looks at the reflection coefficient for a change in the radomes signature over a range of frequencies that indicates a defect. However, this method is both expensive and at times difficult to interpret. More significantly, this reflection-based measurement would be highly susceptible to noise when investigating a low-loss/conductivity material (such as a radome). To obtain higher quality (with less noise), the inside of the radome would need to be backed with some kind of a conductor to increase the amount or reflection. However, even with the conductor backing, this will not solve the issue associated with the curvature of the radome, which would further reduce the amount of the signal reflected. While it shows great promise in applications for characterizing lossy test-pieces (like radar absorbing material), it is not well suited for the present application.

Accordingly, an alternate method was selected for investigation: coplanar stripline resonators. These sensors, formed out of two parallel strips of metal deposited onto a substrate (seen in Figure 3.15), are measured for a shift in their resonant frequency. When the dielec-

tric constant of the surrounding material (i.e. the test-piece) increases, the resonant frequency will decrease in value. This shift is measured to check for the presence of an anomaly in the test-piece. Using this technique carries with it several advantages: small, inexpensive sensors, relatively (compared to the waveguide technique) simple/inexpensive equipment, and easy-to-interpret measurements.

For testing of this technique, the sensor was fabricated and tested on a simulated radome. The sensor was manufactured on FR-4 (standard circuit board material) and scanned over a Rexolite® sandwich structure containing a combination of ceramic alumina and water defects. After two scans of different test-piece configurations, all of the defects were located. However, the shift in resonant frequency resulted from a trading of the peaks for the strongest resonance, rather than a shift in one particular peak. Although a different principle was in use, the measurements obtained yielded images with clear definition of the defect locations.

In addition to the simulated radome, a hand-scan was performed on an actual honeycomb-core radome sample. For this test, the radome was injected with water, filling approximately 5 cells inside the structure. The testing yielded a net shift of 0.23 GHz; unlike the other two tests, this shift resulted solely from a shift in the frequency of one peak and not a trading between two resonances.

With the proof of concept testing complete, a more detailed inquiry should be undertaken into various aspects of this technique. Factors such as sensor geometry (both shape as well as parameters like strip spacing) need to be tested to find the optimal configuration. Probe sensitivity and resolution need to be investigated to ascertain the full capabilities of the technique. Additionally, the sensitivity should be tested using a variety of sensor substrates and correlated with the simulated results to determine the optimal substrate material.

Once the various design aspects are optimized, and full capabilities known, a commercially viable field-deployable inspection unit could be marketed. The sensor and measurement hardware could be assembled into a handheld device for spot testing. For a testing of the full structure, the sensors could be implemented into an array to shorten inspection time. With great simplicity, both in concept and design, coplanar stripline resonators show great promise

for the inspection of aircraft radomes, and potentially countless other NDE measurements on low-loss materials.

Bibliography

[Abegaonkar et al., 1999a] Abegaonkar, M. P., Karekar, R. N., and Aiyer, R. C. (1999a). A microwave microstrip ring resonator as a moisture sensor for biomaterials: application to wheat grains. *Measurement Science and Technology*, 10(3):195–200. 18.

[Abegaonkar et al., 1999b] Abegaonkar, M. P., Karekar, R. N., and Aiyer, R. C. (1999b). Miniaturized nondestructive microwave sensor for chickpea moisture measurement. *Review of Scientific Instruments*, 70(7):3145–3149.

[Atlanta Aerospace, 2008] Atlanta Aerospace (2008). Radome repair. (http://www.atlantaaero.com/dotnetnuke/radomerepair/tabid/142/default.aspx).

[Bahl et al., 1982] Bahl, I. J., Bhartia, P., and Stuchly, S. S. (1982). Design of microstrip antennas covered with a dielectric layer. *IEEE Transactions on Antennas and Propagation*, AP-30(2):314–318.

[Bahl and Stuchly, 1980] Bahl, I. J. and Stuchly, S. S. (1980). Analysis of a microstrip covered with a lossy dielectric. *IEEE Transactions on Microwave Theory and Techniques*, 28(2):104–109.

[Baker-Jarvis et al., 1994] Baker-Jarvis, J., Janezic, M. D., Domich, P. D., and Geyer, R. G. (1994). Analysis of an open-ended coaxial probe with lift-off for nondestructive testing. *IEEE Transactions on Instrumentation and Measurement*, 43(5):711–718.

[Bakhtiari et al., 1993] Bakhtiari, S., Ganchev, S. I., and Zoughi, R. (1993). Open-ended rectangular wave-guide for nondestructive thickness measurement and variation detection of lossy dielectric slabs backed by a conducting plate. *IEEE Transactions on Instrumentation and Measurement*, 42(1):19–24.

[Balageas et al., 2000] Balageas, D., Bourasseau, S., Dupont, M., Bocherens, E., Dewynter-Marty, V., and Ferdinand, P. (2000). Comparison between non-destructive evaluation techniques and integrated fiber optic health monitoring systems for composite sandwich structures. *Journal of Intelligent Material Systems and Structures*, 11(6):426–437. 32 TECHNOMIC PUBL CO INC.

[Balanis, 1989] Balanis, C. A. (1989). *Advanced engineering electromagnetics*. Wiley, New York. .

[Bedair and Wolff, 1992] Bedair, S. S. and Wolff, I. (1992). Fast, accurate and simple approximate analytic formulas for calculating the parameters of supported coplanar wave-guides for (m)mics. *IEEE Transactions on Microwave Theory and Techniques*, 40(1):41–48.

[Blatz et al., 2007] Blatz, S., Barnard, D., and Hsu, D. (2007). Capacitive detection of water in radomes. Technical report.

[Bois et al., 1999] Bois, K. J., Benally, A. D., and Zoughi, R. (1999). Multimode solution for the reflection properties of an open-ended rectangular waveguide radiating into a dielectric half-space: The forward and inverse problems. *IEEE Transactions on Instrumentation and Measurement*, 48(6):1131–1140.

[C-LEC Plastics, 2008] C-LEC Plastics (2008). Rexolite information - http://www.rexolite.com/list.html.

[Carlsson and Gevorgian, 1999] Carlsson, E. and Gevorgian, S. (1999). Conformal mapping of the field and charge distributions in multilayered substrate cpw's. *IEEE Transactions on Microwave Theory and Techniques*, 47(8):1544–1552.

[Chang et al., 1997] Chang, C. W., Chen, K. M., and Qian, J. (1997). Nondestructive determination of electromagnetic parameters of dielectric materials at x-band frequencies using a waveguide probe system. *IEEE Transactions on Instrumentation and Measurement*, 46(5):1084–1092.

[CNDE, 2007] CNDE (2007). Quantitative inspection techniques for assessing aging military aircraft - progress report (jun-aug 2007). Technical report, Center for Nondestructive Evaluation.

[Collins, 2008] Collins, R. (2008). Twr-850/wxr-840 weather radar systems specifications.

[Demenicis et al., 2007] Demenicis, L. S., Lima, R. A. A., Conrado, L. F. M., Margulis, W., and Carvalho, M. C. R. (2007). A cpw linear resonator method for the microwave characterization of high dielectric constant films. *Microwave and Optical Technology Letters*, 49(3):521–524.

[Ganchev et al., 1996] Ganchev, S. I., Zoughi, R., Huber, C., Runser, R. J., and Ranu, E. (1996). Microwave method for locating surface slot/crack tips in metals. *Materials Evaluation*, 54(5):598–603.

[Ghione and Naldi, 1987] Ghione, G. and Naldi, C. U. (1987). Coplanar waveguides for mmic applications - effect of upper shielding, conductor backing, finite-extent ground planes, and line-to-line coupling. *IEEE Transactions on Microwave Theory and Techniques*, 35(3):260–267.

[Gupta et al., 1979] Gupta, K. C., Garg, R., and Bahl, I. J. (1979). *Microstrip lines and slotlines*. Artech House, Dedham, Mass.

[Hsu, 2007] Hsu, D. (2007). Characterization of saint gobain radome structure. Technical report.

[Hu et al., 2006] Hu, J. Q., Sligar, A., Chang, C. H., Lu, S. L., and Settaluri, R. K. (2006). A grounded coplanar waveguide technique for microwave measurement of complex permittivity and permeability. *IEEE Transactions on Magnetics*, 42(7):1929–1931.

[Itoh, 1974] Itoh, T. (1974). New method for measuring properties of dielectric materials using a microstrip cavity. *IEEE Transactions on Microwave Theory and Techniques*, MT22(5):572–576.

[Joshi et al., 1997] Joshi, K. K., Abegaonkar, M., Karekar, R. N., and Aiyer, R. C. (1997). Microstrip ring resonator as a moisture sensor for wheat grains. In Koepf, G. A., Jelks, C., Huebner, D., and Donovan, J. J., editors, *1997 IEEE MTT-S International Microwave Symposium Digest, Vols I-III - High Frequencies in High Places*, IEEE MTT-S International Microwave Symposium Digest, pages 1679–1682.

[Kent, 1972] Kent, M. (1972). Use of strip-line configurations in microwave moisture measurement. *Journal of Microwave Power*, 7(3):185–193.

[Kent and Kohler, 1984] Kent, M. and Kohler, J. (1984). Broad-band measurement of stripline moisture sensors. *Journal of Microwave Power and Electromagnetic Energy*, 19(3):173–179.

[Khanfar et al., 2003] Khanfar, A., Abu-Khousa, M., and Qaddoumi, N. (2003). Microwave near-field nondestructive detection and characterization of disbonds in concrete structures using fuzzy logic techniques. *Composite Structures*, 62(3-4):335–339.

[Kharkovsky et al., 2006] Kharkovsky, S., Ryley, A. C., Stephen, V., and Zoughi, R. (2006). Dual-polarized microwave near-field reflectometer for non-invasive inspection of carbon fiber reinforced polymer (cfrp) strengthened structures. In *2006 IEEE Instrumentation and Measurement Technology Conference Proceedings, Vols 1-5*, IEEE Instrumentation and Measurement Technology Conference, Proceedings, pages 2108–2111. Kharkovsky, Sergey Ryley, Adam C. Stephen, Vivian Zoughi, Reza 23rd IEEE Instrumentation and Measurement Technology Conference APR 24-27, 2006 Sorrento, ITALY.

[Kim et al., 2006] Kim, K. B., Kim, J. H., Lee, C. J., Noll, S. H., and Kim, M. S. (2006). Simple instrument for moisture measurement in grain by free-space microwave transmission. *Transactions of the ASABE*, 49(4):1089–1093.

[Matthaei et al., 1990] Matthaei, G. L., Kiziloglu, K., Dagli, N., and Long, S. I. (1990). The nature of the charges, currents, and fields in and about conductors having cross-sectional dimensions of the order of a skin depth. *IEEE Transactions on Microwave Theory and Techniques*, 38(8):1031–1036.

[Mautz and Harrington, 1978] Mautz, J. R. and Harrington, R. F. (1978). Transmission from a rectangular waveguide into half space through a rectangular aperture. *IEEE Transactions on Microwave Theory and Techniques*, 26(1):44–45. 5.

[Nadakuduti et al., 2006] Nadakuduti, J., Chen, G., and Zoughi, R. (2006). Semiempirical electromagnetic modeling of crack detection and sizing in cement-based materials using near-field microwave methods. *IEEE Transactions on Instrumentation and Measurement*, 55(2):588–597.

[Nadakuduti et al., 2003] Nadakuduti, J., Zoughi, R., Ying, X., and Chen, G. (2003). Near-field microwave techniques for detecting stress-induced cracks in cement-based materials. In Wu, Z. S. and Abe, M., editors, *Structural Health Monitoring and Intelligent Infrastructure, Vols 1 and 2*, pages 711–718. 1st International Conference on Structural Health Monitoring and Intelligent Infrastructure NOV 13-15, 2003 TOKYO, JAPAN.

[Napert, 1999] Napert, G. (1999). What you should know about radomes. (http://www.amtonline.com/article/article.jsp?id=843).

[Napoli and Hughes, 1971] Napoli, L. S. and Hughes, J. J. (1971). Simple technique for accurate determination of microwave dielectric constant for microwave integrated circuit substrates. *IEEE Transactions on Microwave Theory and Techniques*, MT19(7):664–665.

[Nissen, 2005] Nissen, J. (2005). Development of innovative new microwave techniques for nondestructive inspective (ndi) using existing microwave coating thickness gage. Technical report, Bell Helicopter - Textron, Inc.

[Olyphant and Ball, 1970] Olyphant, M. and Ball, J. H. (1970). Strip-line methods for dielectric measurements at microwave frequencies. *IEEE Transactions on Electrical Insulation*, EI 5(1):26–27.

[Press, 2004] Press, C. (2004). *CRC handbook of chemistry and physics*. CRC Press [etc.], Cleveland, Ohio.

[Rao, 1989] Rao, B. (1989). Free-space millimeter-wave measurement of the complex dielectric constant of radome materials using nonlinear least-squares analysis. In *IEEE Antennas and Propagation Society International Symposium*.

[Root and Kaufman, 1992] Root, L. F. and Kaufman, I. (1992). Noncontacting low-cost instrument for film thickness measurement. *IEEE Transactions on Instrumentation and Measurement*, 41(6):1014–1019.

[Saka et al., 2002] Saka, M., Ju, Y., Luo, D. Y., and Abe, H. (2002). A method for sizing small fatigue cracks in stainless steel using microwaves. *JSME International Journal Series a-Solid Mechanics and Material Engineering*, 45(4):573–578.

[Saleh et al., 2003] Saleh, W., Qaddoumi, N., and Abu-Khousa, M. (2003). Preliminary investigation of near-field nondestructive testing of carbon-loaded composites using loaded open-ended waveguides. *Composite Structures*, 62(3-4):403–407.

[Sarabandi and Li, 1997] Sarabandi, K. and Li, E. S. (1997). Microstrip ring resonator for soil moisture measurements. *IEEE Transactions on Geoscience and Remote Sensing*, 35(5):1223–1231.

[Stewart et al., 2007] Stewart, J., Havrilla, M., Berrie, J., Kornbau, N., Stenholm, G., and Albert, A. (2007). Material characterization using a hand-held network analyzer.

[Stewart and Havrilla, 2006] Stewart, J. W. and Havrilla, M. J. (2006). Electromagnetic characterization of a magnetic material using an open-ended waveguide probe and a rigorous full-wave multimode model. *Journal of Electromagnetic Waves and Applications*, 20(14):2037–2052. Stewart, J. W. Havrilla, M. J.

[Tan et al., 2004] Tan, C. Y., Chen, L. F., Chong, K. B., and Ong, C. K. (2004). Nondestructive microwave permittivity characterization of ferroelectric thin film using microstrip dual resonator. *Review of Scientific Instruments*, 75(1):136–140.

[Tantot et al., 1997] Tantot, O., Chatard-Moulin, M., and Guillon, P. (1997). Measurement of complex permittivity and permeability and thickness of multilayered medium by an open-ended waveguide method. *IEEE Transactions on Instrumentation and Measurement*, 46(2):519–522.

[Tsuji et al., 2007] Tsuji, M., Tsuda, S., Nishikawa, T., Wakino, K., and Kitazawa, T. (2007). Evaluation method of high-permittivity materials in microwave region using coplanar waveguide. *Electronics and Communications in Japan Part Ii-Electronics*, 90(3):17–25. Tsuji, Masatoshi Tsuda, Shotaro Nishikawa, Toshio Wakino, Kikuo Kitazawa, Toshihide.

[Waldo et al., 1997] Waldo, M. K., Kaufman, I., and El-Ghazaly, S. (1997). Coplanar waveguide technique for measurement of dielectric constant or thickness of dielectric films. In Koepf, G. A., Jelks,

C., Huebner, D., and Donovan, J. J., editors, *1997 IEEE MTT-S International Microwave Symposium Digest, Vols I-Iii - High Frequencies in High Places*, IEEE MTT-S International Microwave Symposium Digest, pages 1339–1342.

[Wegman and Tullos, 1992] Wegman, R. F. and Tullos, T. R. (1992). *Handbook of adhesive bonded structural repair*. Noyes Publications, Park Ridge, N.J., U.S.A. 91046660 (OCoLC)25048565 by Raymond F. Wegman and Thomas R. Tullos. ill. ; 25 cm. Includes bibliographical references and index.

[Yogi et al., 1998] Yogi, R. A., Gangal, S. A., Aiyer, R. C., and Karekar, R. N. (1998). Microwave ring resonator as a novel bio-material moisture sensor. *Sensors and Actuators B-Chemical*, 50(1):38–44.

[Yogi et al., 2002] Yogi, R. A., Parolia, R. S., Karekar, R. N., and Aiyer, R. C. (2002). Microwave microstrip ring resonator as a paper moisture sensor: study with different grammage. *Measurement Science and Technology*, 13(10):1558–1562.

[Yoshitomi and Sharobim, 1994] Yoshitomi, K. and Sharobim, H. R. (1994). Radiation from a rectangular wave-guide with a lossy flange. *IEEE Transactions on Antennas and Propagation*, 42(10):1398–1403.